Preprints (www.preprints.org) | NOT PEER-REVIEWED | Posted: 13 September 2022 doi:10.20944/preprints202209.0170.v1

Article

Polymorphism and Perfection in Crystallization of Hard Sphere Polymers

Miguel Herranz, Katerina Foteinopoulou, Nikos Ch. Karayiannis*, and Manuel Laso*

Institute for Optoelectronic Systems and Microtechnology (ISOM) and Escuela Técnica Superior de Ingenieros Industriales (ETSII), Universidad Politécnica de Madrid (UPM), José Gutierrez Abascal 2, 28006 Madrid, Spain; miguel.herranzf@upm.es (M.H.); k.foteinopoulou@upm.es (K.F.)

* Correspondence: (N.K.) n.karayiannis@upm.es; Tel.: +34-910677318; (M.L.) m.laso@upm.es; Tel.: +34-910677320

Abstract: We present results on the spontaneous crystallization of freely-jointed polymers of hard spheres obtained in an unprecedentedly long Monte Carlo (MC) simulation on a system of 54 chains of 1000 monomers. Starting from a purely amorphous configuration and after a transitory dominance of the hexagonal closed packed (HCP) polymorph, the system crystallizes in a final, stable, face centered cubic (FCC) crystal of very high perfection. Through refined metrics we gauge the degree of ordering and identify the regions of the phase transition and the corresponding morphologies. An analysis of chain conformational characteristics, of the spatial distribution of monomers and of the volume accessible to them shows that the phase transition is caused by an increase in translational entropy that is larger than the loss of conformational entropy of the chains in the crystal compared to the amorphous state. Polymer chains in the crystal adopt ideal random walk statistics as their great length renders local conformational details imposed by the geometry of the FCC crystal irrelevant.

Key words: n/a; Hard Sphere; Crystallization; Entropy-driven phenomena; packing; polymer; molecular simulation; phase transition; face centered-cubic; hexagonal close packed; random walk; colloids; crystal perfection

1. Introduction

The importance of crystallization in physics, materials, life science and technology cannot be sufficiently emphasized. It plays a major role in the pharmaceutical industry [1], the storage of clean fuels such as hydrogen [2] and catalytic processes [3] among other industrial processes [4]. Besides, ordered structures of polymer-based physical and chemical systems are of paramount importance in the development of novel solar cells [5], semiconductors [6], biological materials [7] or conventional plastics [8]. Due to its high complexity crystallization remains a topic surrounded frequently by scientific controversy and debate, especially since the classical view is considered too simple to cover a wide range of physical systems and conditions [9–11].

The basics of crystallization have been studied, among other systems, on simple spherical colloids due to their suitability as macroscopic model system as they can be easily probed, and bear properties and characteristics which can be tailored within wide ranges [12,13]. Extensive and careful experimental work has unmistakably demonstrated the difficulty of obtaining quite perfect crystals [14–16].

The identification of competing crystal structures of colloidal crystals has been carried out by methods like fluorescence confocal scanning laser microscopy [17], small-angle synchrotron x-ray diffraction [18], laser scanning confocal microscopy [15] or light scattering [19]. In many of these experimental studies the random hexagonal close packed (rHCP) structure prevails as the final ordered structure. It has also been shown that gravity and microgravity play a significant role in the crystallization of colloids [14,20–23]. In many cases, aging of structures of colloidal spheres leads to a slow transition from the rHCP morphology to the theoretically expected, and thermodynamically more stable, face centered cubic (FCC) structure of varying degrees of perfection[24–26].

These experimental efforts have been accompanied by numerous analytical and simulation works [27–33]. The experimentally observed sluggishness of the rHCP→FCC

© 2022 by the author(s). Distributed under a Creative Commons CC BY license.

Preprints (www.preprints.org) | NOT PEER-REVIEWED | Posted: 13 September 2022 doi:10.20944/preprints202209.0170.v1

transformation also appears in simulations [34]. Obtaining a stable crystal of well defined crystalline, close-packed character is still a very challenging task even for the simplest possible system realization, that of monomeric hard spheres (HS). The Kepler conjecture, as further extended by Gauss for regular lattices and eventually proven by Hales and coworkers in [35], states that for a 3D packing of hard spheres the densest possible configuration corresponds to the hexagonal close packed (HCP) or the FCC crystal arrangements, both leading to a space filling fraction of approximately 0.7404.

This competition of the close packed HCP and FCC crystals has been studied from the perspectives of nucleation [36–38], entropy (free energy) difference [34,39–43], geometric arguments [44] and Ostwald's Rule of Steps [45], among others. Theoretical works have been accompanied by simulations as in [43,44,46–49].

Available estimates of the entropy (directly proportional to free energy for hard spheres) demonstate an advantage of FCC against HCP which ranges between 9×10^{-4} and 50×10^{-4} per particle (expressed in terms of Boltzmann's constant k) [39,41,43,47,50]. The variation is attributable primarily to the methods used and to a lesser extent to the conditions at which it is calculated: ΔS seems to vary only by about $25 - 30\%$ between the melting transition and the maximum density. It is the smallness of this value that is responsible for the difficulty of obtaining neat crystals of the stable FCC polymorph, both experimentally and computationally.

As a consequence, it is not surprising that the vast majority of isochoric simulations, starting from predominately amorphous monomeric HS packings, result in highly defective ordered structures of rHCP character [28,30,51,52]. The body of simulation works where FCC-like crystals are obtained is very limited [53,54]. The investigation of the FCC-HCP competition has been extended in simulations to the study of the effect of gravity [55], crystallization from seeds [37], sedimentation [56], template-assisted crystallization [57–59] or crystallization on surfaces and interfaces [60–62] .

Research studies addressing the corresponding problem for polymers (chains) made of hard spheres are even sparser. Experiments on linear polymers of HS-like monomers are even more challenging than for monomeric systems. In spite of granular, colloidal or droplet polymers being significantly less explored than the "traditional" ones, over the years there have been significant advances from several research groups in their synthesis and characterization [63–67].

Theoretical and modeling works are of major importance in the study of crystallization of hard sphere chains [68,69]. From the perspective of simulation, emphasis is placed on the phase transition of semi-flexible [70–72] or flexible [73,74] chains of hard spheres, while recently it was demonstrated that the use of block copolymers leads to HCP stable phases [75–77]. The stabilization of HCP colloidal structures has been investigated through insertion of polymers [78,79]. In spite of these advances, crystal perfection and relative stability of crystals of long, entangled HS polymers is still considered an uncharted territory.

This is not surprising as the study of polymer crystallization by simulation, either for chemically realistic macromolecular systems or for simplified analogs, is especially challenging because of the large molecular size leading to a wide spectrum of characteristic lengths and relaxation times. Accordingly, studying nucleation, growth and perfection of crystals requires efficient and robust sampling both at short- and long-range. The very long relaxation times are also responsible for the difficulty of preparing crystals of polymers of reasonable quality in the laboratory. It is no exaggeration to say that high-quality bulk polymer crystals with a well defined habit remain a laboratory curiosity, although a very valuable one for they have provided fundamental information on the unique characteristics of polymer crystallization. Most crystalline and semicrystalline polymers consist of huge assemblies of imperfect crystals, often and unavoidably combined with amorphous regions.

The previous remarks should not detract from the importance of understanding the mechanisms and dynamics of athermal polymer crystallization. Focusing on the computational work, the large size and concomitant sluggish dynamics of polymers present researchers with unusual challenges. Major conformational rearrangements involving the slowest modes, that play a key role in the formation of polymer crystals, can be well beyond the reach of deterministic methods.

Monte Carlo (MC) methods do not suffer from the slow dynamics associated with large molecular size like in Molecular Dynamics (MD). Conformational sampling in MC does not follow a deterministic, dynamic path between successive system states. The most advanced MC methods are precisely based on highly non-physical moves that allow rapid equilibration and robust sampling in configuration space [80,81]. This advantage is obviously offset by the loss of dynamic information, although methods such as Kinetic Monte Carlo (KMC) [82,83] do offer a reasonable compromise when the rates of individual events are known in advance.

In addition, developing MC methods which correctly and efficiently sample polymer conformational space is not a trivial matter. The difficulty presented to MD methods by the extremely wide range of polymer relaxation times is replaced in MC by the difficulty of designing moves which may effect not only small scale but also large-scale chain rearrangements. Nor surprisingly, the complexity of the problem is greatly increased if the goal is to study multi-chain, polymer systems at very high densities, above the melting transition where crystal nucleation and growth takes place.

In spite of these difficulties, a wide variety of increasingly more efficient MC methods have been developed over the last decades [80,81,84–90]. The work to be reported in this manuscript is based on a powerful suite of advanced MC moves [91] which has enabled us in the past to observe the entropy-driven athermal polymer crystallization for the first time [73] and to identify and analyze the factors that affect the phenomenon, including chain length and its distribution [73,92], the presence of bond gaps or tangency [93] and confinement in one [94] or all three [95] dimensions.

In the present contribution unprecedentedly long Monte Carlo simulations allow to study polymorphism and perfection in very long chains of hard spheres. These isochoric simulations start from an isotropic amorphous packing and, after a transient dominance of the HCP polymorph and the successive establishment of rHCP morphologies of various levels of ordering, reach eventually a final FCC crystalline state of remarkable perfection.

In a companion paper [96] we support the computationally observed stability of the FCC polymorph by means of quantitative analytic calculations.

2. Methodology

We adopt the freely jointed model of linear chains comprised of hard sphere monomers with uniform diameter σ, which is taken as unit length. The pair-wise energy, $u_{HS}(r_{ij})$ is given by the equation:

$$u_{HS}(r_{ij}) = \begin{cases} 0, r_{ij} \geq \sigma \\ \infty, r_{ij} < \sigma \end{cases} \tag{1}$$

where r_{ij} is the distance between the centres of monomers i and j. This is the only type of interaction between all monomer pairs; neither bending nor torsional potentials are applied to successive monomers along the chain backbone. For numerical convenience, bond lengths, b_{len}, are allowed to vary uniformly in the interval $b_{len} \in [\sigma, \sigma + db]$, where db is the maximum bond tolerance (gap) between two successive monomers, and it is set equal to 0.13σ. $\langle b_{len} \rangle$ corresponds to the average bond length, where $\langle \quad \rangle$ denote average over all bonds for a given set of system configurations (frames).

The simulations are conducted using the *Simu-D* simulator-descriptor suite [91] in the isochoric, semigrand ensemble $[VTN_{sites}\mu^*]$. In the $[VTN_{sites}\mu^*]$ ensemble [97] underlying the present calculation, chain lengths obey a given distribution, which is enforced by means of the chemical potentials μ^*, and are allowed to fluctuate within a predetermined range. The practical implementation for the uniform and Flory chain length distributions is explained in detail in the Appendix of Ref. [98]. For athermal systems, the formal conjugate pair of variables T, U is inactive (see [97] for details).

Preprints (www.preprints.org) | NOT PEER-REVIEWED | Posted: 13 September 2022 doi:10.20944/preprints202209.0170.v1

The system under study is comprised of $N = 54$ chains of average size $l_{av} = 1000$, leading to a total of $N_{sites} = 54000$ monomers or sites. In this isochoric, semigrand ensemble, total volume V, total number of monomers N_{sites} and the spectrum of chemical potentials are specified. Here, a flat (uniform) chain length distribution is chosen within the interval $[l_{min}, l_{max}]$ with $l_{min} = 600$ and $l_{max} = 1400$, as a requirement for the application of specific algorithms (see below). As will be shown in the results section, this chain length range lies deep in the polymeric regime. The uniform distribution is selected over the Flory one as it allows for robust sampling of the long-range chain characteristics in the whole interval $[l_{min}, l_{max}]$.

The core of the Monte Carlo suite consists of chain-connectivity-altering moves (CCAMs), which allow the robust equilibration of the system even at very high volume fractions [98–100], up to the maximally random jammed state [101]. CCAMs are accompanied by more standard MC moves. The following attempt probabilities for each move have been used: (i) rotation (10%), (ii) reptation (10%), (iii) flip (34.8%), (iv) intermolecular reptation (25%), (v) configurational bias (20%), (vi) simplified end-bridging, sEB (0.1%) and (vii) simplified intermolecular end-bridging, sIEB (0.1%). Neither cluster [102] nor identity exchange moves [91] are incorporated here.

The initial configuration is generated through progressive shrinkage of a very dilute configuration that meets the constraints imposed by chain connectivity until a desired packing density (volume fraction) of $\varphi = 0.56$ is reached [91], or $\varphi^* = \frac{\varphi}{0.7405} = 0.756$ relative to the maximum compacity of the FCC or HCP crystals. The cubic simulation cell is subjected to periodic boundary conditions in all directions corresponding to a bulk and unconstraint system. Due to the high density a configurational MC bias pattern is used throughout with $n_{dis} = 50$ candidate configurations being attempted per local move as explained in detail in [91,101].

The simulation is carried out over 1.4×10^{12} MC steps, and system configurations are recorded every 10^8 MC steps. Due to the very large system size, the time required to establish crystal perfection was close to 4 years of continuous wall-clock CPU time on a single Intel i5 processor with 32 Gb of memory.

The core post-processing tool of the work is the Characteristic Crystallographic Element (CCE norm), as implemented in the descriptor part of the *Simu-D* software [91]. This descriptor of structural order gauges both radial and orientational similarity of the local environment of a monomer with respect to reference crystals in two or three dimensions [103,104].

To this end, a tessellation into Voronoi cells (VC) around all monomers of the system is carried out (by means of the voro++ software [105]) and as a first step the closest neighbors are identified for each monomer. The CCE norm for each monomer is then computed by carrying out the geometric symmetry operations of the point group of several candidate reference crystals (e.g. FCC and HCP) and evaluating the deviation from geometric invariance.

The CCE norm, ε_j^X is assigned to each monomer, j, which is a measure of the deviation of its environment with respect to each reference crystal, X. The closer the value of the norm to zero, the greater the similarity of the monomer's environment to the reference crystal. A type is assigned to each monomer depending on its structural similarity to a given characteristic point group (crystalline or not) by checking its CCE-norm against a threshold value, set here at $\varepsilon^{thres} = 0.3$. This value was found to ensure selective discrimination among competing polymorphs for the system at hand.

We calculate this CCE norm for each monomer at each MC frame, independently of which chain they belong to, in order to quantitatively analyze the evolution of crystallinity and the competition among polymorphs [103,104].

System configurations were tested against all reference 3-D crystals implemented in *Simu-D*: hexagonal close packed (HCP), face centered cubic (FCC), body centered cubic (BCC), simple hexagonal (HEX), but also with respect to the non-crystallographic fivefold

(FIV) local symmetry [104,106]. Only four different types of monomers were detected along the entire simulation:

- monomers with first neighbors whose arrangement conforms to the point symmetry group $m3m$ of the face centered cubic crystal (FCC sites),
- monomers with first neighbors whose positions conform to the point group $\bar{6}m2$ of the hexagonal close packing crystal (HCP sites),
- monomers whose first neighbors conform to the point group 5 of a non-crystallographic fivefold axis (FIV sites),
- monomers with first neighbors that are not arranged according to any kind of symmetry (apart from the identity E), either crystallographic or non-crystallographic (amorphous, denoted AMO).

In all analyzed sites and over all recorded configurations (frames) no instances of sites with BCC or HEX symmetry were found.

Based on the CCE-norm, an order parameter, $S^X \in [0, 1]$ for each reference point group type $X \in$ [HCP, FCC, FIV] was defined as:

$$S^X = \int_0^{\varepsilon^{thres}} P(\varepsilon^X)\, d\varepsilon^X$$

where $P(\varepsilon^X)$ is the probability distribution function for the CCE norm of the X reference point group symmetry. In addition, $S^{AMO} = 1 - S^{HCP} - S^{FCC} - S^{FIV}$. Given that only FCC and HCP crystalline sites exist in the system configurations, and as neither AMO nor FIV sites contribute, the total crystallinity is given simply by:

$$\tau_c = S^{FCC} + S^{HCP}$$

3. Results

As stated earlier, the simulation reached 1.4×10^{12} MC steps, with only one configuration every 10^8 MC steps being stored, for a total of 14,000 configurations (or *frames* or *snapshots*). This separation between successive frames was found to be sufficient to ensure frame decorrelation. The number of 10^8 MC steps between successive frames correspond to an average of 1.85×10^6 MC moves per chain between successive frames.

3.1. Evolution of crystallinity

Starting from a purely amorphous, statistically homogeneous configuration, the *Simu-D* MC suite is able to evolve the system through intermediate states until a stable polymorph of remarkable perfection is formed. The evolution of the individual order parameters and total crystalinity as a function of MC steps is shown in Figs. 1 and 2. The intermediate states that appear before the MC calculation settles in an equilibrated FCC polymorph are characterized by a spatial distribution of regions of varied crystallographic nature, which evolve both in size and perfection along the simulation.

Fig. 1 covers the whole simulation trajectory while Fig. 2 focuses on the early part. The fraction of amorphous sites, S^{AMO}, quantifies the degree of disorder in the system, to be contrasted against the degree of crystallinity, τ_c.

For simplicity, and based on these figures, the system evolution can be conveniently split in four qualitatively different regions (Fig. 1), numbered I through IV. Region I: MC steps 1×10^8 - 1.5×10^{11} (or equivalently frames 1 - 1500); II: MC steps 1.5×10^{11} - 5.3×10^{11} (frames 1500 - 5300); III: 5.3×10^{11} - 9.1×10^{11} (frames 5300 - 9100); IV: 9.1×10^{11} - 1.4×10^{12} (frames 9100 - 14000). From now on, except if otherwise state, frame numbers are quoted rounded to the nearest 100, and are understood to be approximate only, just as the boundaries between regions are not strictly sharp.

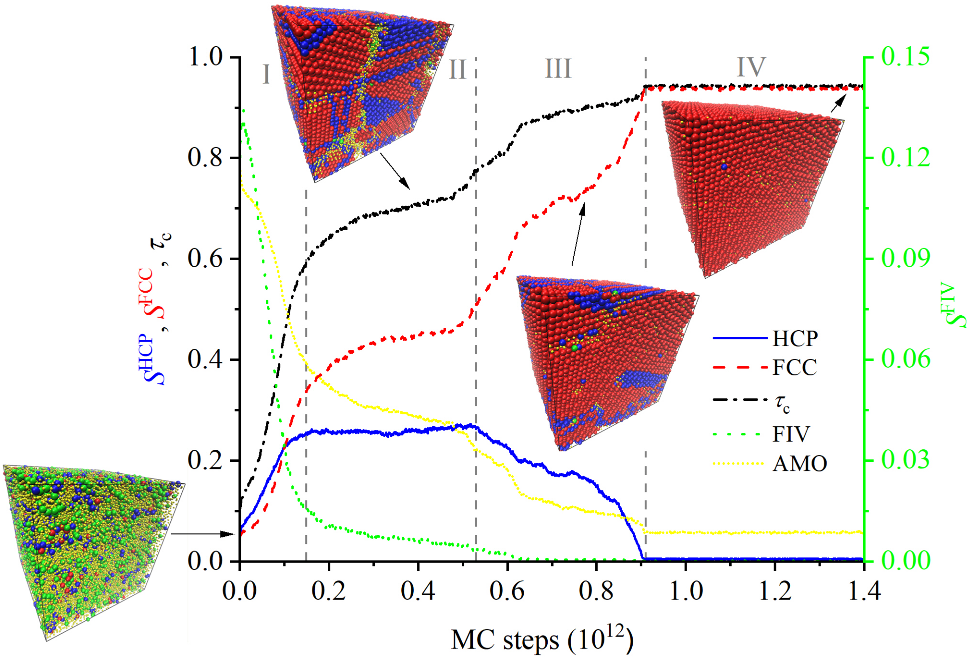

Figure 1. Evolution of the number fractions, $S^X, X \in$ [HCP, FCC, FIV, AMO] of sites of each type along the MC calculation. Fivefold order parameter is shown on the right y-axis. Roman numerals and dashed vertical lines denote the four distinct regions in the evolution of the morphology (see main text). Also shown are perspective visualizations of representative frames in the four regimes. Spherical monomers are colored following the same convention as the curves according to their point group symmetry/crystal type: HCP: blue, FCC: red , FIV: green, AMO: yellow. The corresponding curves are represented by solid (HCP), dashed (FCC), dotted (FIV), dashed-dotted (τ_c) and short-dotted (AMO) styles. The correspondence of the color scheme and line style to the HCP/FCC/FIV structures of this figure is valid for the rest of the manuscript.

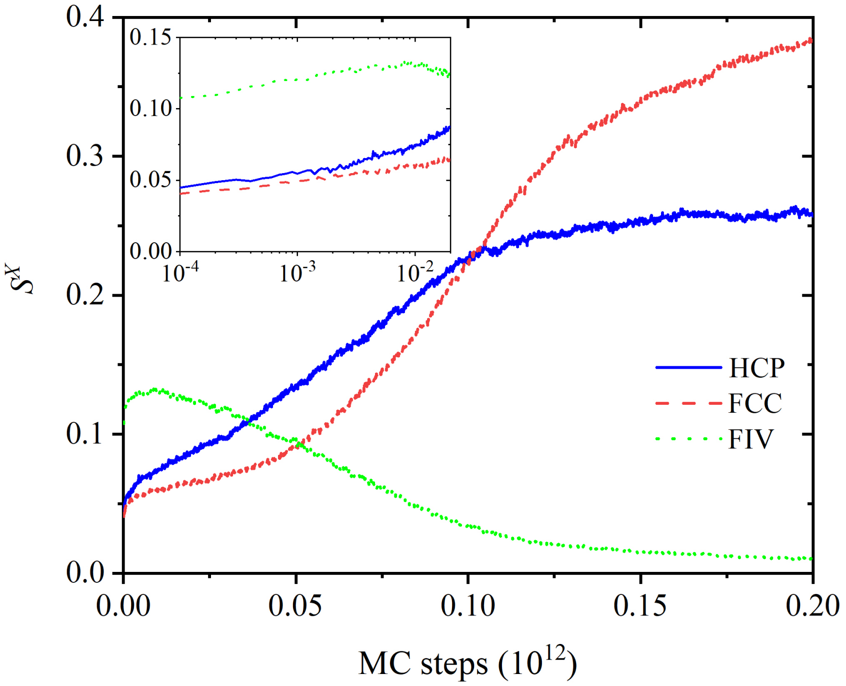

Figure 2. Early evolution of site fractions $S^X, X \in$ [HCP, FCC, FIV] in the first 2000 frames (2×10^{11} MC steps). Inset: zoom on the first 200 frames (2×10^{10} MC steps) in log-linear scale.

Preprints (www.preprints.org) | NOT PEER-REVIEWED | Posted: 13 September 2022 doi:10.20944/preprints202209.0170.v1

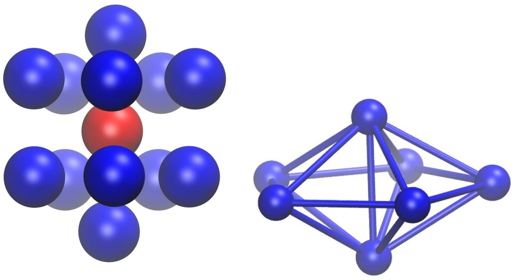

Figure 3. (Left panel) First neighbor shell for a representative site of FIV character ($\varepsilon_{14717}^{FIV} = 0.05$) in frame 1276 (Region I) of the MC simulation. The 12 neighbors atoms are marked in blue and the reference atom in red. Ten 4-monomer tetrahedra share a common fivefold axis and the reference site (marked in red).The non-crystallographic fivefold axis runs through the topmost, the middle (red) and the bottom-most sites, i.e. vertically on the page. (Right panel) The corresponding pentagonal bipyramid. Image created with the VMD visualization software [109].

In Region I, starting from the initial amorphous configuration, a rapidly [1] growing number of monomers spontaneously develop crystalline character, as evidenced by the steep drop in the AMO curve and the simultaneous growth of the number of FCC and HCP sites. As a matter of fact, 8.4% of all sites already have definite HCP or FCC character, and 11% show FIV character in the very first frame (10^8 MC steps). This is the reason for the curves in Figs. 1 and 2 apparently not starting at 0 (HCP, FCC, FIV) or 1 (AMO), and is a consequence of the great length of the calculation: alone in the first frame, 1.85×10^3 MC moves have been carried out on average for each of the $N_{sites} = 54000$ monomers.

These observations are also qualitatively consistent with the degree of ordering found in simulations of random packings of monomeric hard spheres at concentrations above the melting transition [51,52], where the population of fivefold sites initially exceeds the sum of sites with HCP or FCC character. This initial copiousness of sites with FIV symmetry has repeatedly been observed both in simulations of crystallization of single (monomeric) [51,52] as well as in polymeric [107,108] systems of hard spheres .

After growing to approximately $\approx 10\%$ within the first frame, the noncrystallographic FIV population remains largest in the first few frames, then drops steadily in parallel with the population of AMO sites, in favor of FCC and HCP sites.

The initial nucleation sites are transformed into compact [2] assemblies of four sites of very approximate tetrahedral shape. The appearance of FIV sites is favored by the ease with which these four-monomer tetrahedra can be arranged in a variety of almost compact clusters which fill space efficiently at a small scale, like the pentagonal bipyramid shown on the right panel of Fig. 3.

The reason for the metastability of such arrangements is primarily geometric: at the smallest scale, five 4-site tetrahedra can be arranged around a common axis so that they share an edge and build a 7-monomer bipyramid of almost, but not quite, exact fivefold symmetry, the fivefold axis being the common edge. By ordered accretion of further elemental tetrahedra, structures of pentagonal symmetry and varying complexity [110–113] appear as metastable, long-lived morphologies in simulations.

The left panel of Fig. 3 shows the first neighbor shell of a representative site of FIV character ($\varepsilon_{14717}^{FIV} = 0.05$), as spontaneously formed in Region I. Two of the pentagonal bipyramids described above share one site (marked in red in Fig. 3) and also have a common, single fivefold axis, running vertically on the paper in this figure. This 13-site structure and other similar arrangements [114] are favored with respect to local disorder

---

[1] in the rest of the manuscript we will use kinetic terms such as “rate”, “fast” etc for brevity and simplicity in order to describe the evolution of the system measured in terms of MC steps but without claiming any truly kinetic or dynamic meaning.

[2] “compact” in the sense that the four monomers form a regular tetrahedron with minimal inter-site distance.

Preprints (www.preprints.org) | NOT PEER-REVIEWED | Posted: 13 September 2022 doi:10.20944/preprints202209.0170.v1

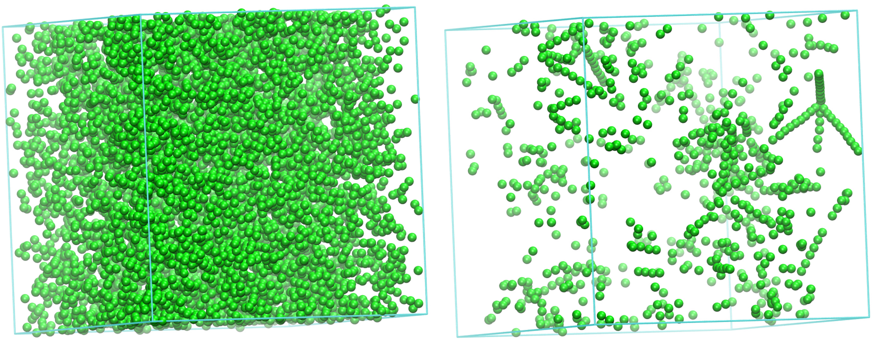

Figure 4. Spatial distribution of FIV sites in (Left): Region I (frame 125, $S^{FIV} = 0.129$) and (Right): Region II (frame 1622, $S^{FIV} = 0.014$). Image created with the VMD visualization software [109].

because they lead to a localized increase in available volume and in system translational entropy.

Initially, FIV sites appear abundantly and randomly distributed in the simulation cell, but as their population subsequently decreases they develop a remarkably non-homogeneous distribution in space. The left panel of Fig. 4 shows this spatial distribution of sites with FIV symmetry at a configuration within Region I (frame 125). At this stage most of the numerous FIV sites ($S^{FIV} = 0.129$) are still isolated, although the first traces of linear assemblies of FIV sites are already visible. At a later stage of the simulation (frame 1622, early in Region II), as can be seen in the right panel of Fig. 4, the FIV population is significantly lower ($S^{FIV} = 0.014$) and the majority is organized in specific geometric patterns.

The most prevalent and long-lived among these arrangements are linear asssemblies of FIV sites, which are formed as the tetrahedra in Fig. 3 grow by further accretion of sites. Such linear assemblies of FIV that survive into Region II (see below) are entirely analogous to those observed in MD simulations [112,113].

Pentatwin formation is especially favorable due to the similarity between the pentagonal 72° angle and the value of the dihedral angle 70.53° between two faces of the regular tetrahedron. A gap of only $360° - 5 \times 70.53° = 7.35°$ is left when five equally sized tetrahedra share an edge. Such tetrahedral nuclei appear easily by site accretion around the initial, minimal, 4-monomer tetrahedra of Region I, and five such clusters form an almost perfect pentagonal dipyramid. Interestingly, the small angular mismatch of 7.35° is not taken up by non-crystalline monomers as five equal, wedge-like gaps $\approx \frac{1}{5}7.35°$ placed among the five twins, but the whole mismatch remains confined between two adjacent tetrahedra which are less perfect than the remaining three (see rightmost two sectors in the middle panel of Fig. 5).

However, because of the impossibility of compactly tesselating 3D space using regular tetrahedra [115], noncrystallographic FIV sites can only be a transient phenomenon and tend to disappear in favor of compact structures of crystallographic symmetry. The simulation does indeed evolve the system into configurations of higher crystallographic FCC or HCP character. Consequently, a marked decrease in the number of FIV sites is observed in region I, while total crystallinity increases rapidly. A video showing the FIV sites evolution in Regions I and II can be found in the Supplemental Material [3].

Furthermore, the rates of growth of both FCC and HCP crystalline sites are roughly similar in Region I, as shown in both main and inset panels of Fig. 2. The main reason for the approximately equal initial rates of growth is the high geometric similarity in the structures of HCP and FCC: both can be obtained by the stacking of two-dimensional, hexagonally close-packed layers, differing only in the stacking sequence, . . . A-B-A-B-. . . for HCP and . . . A-B-C-A-B-C-. . . for FCC. In the case of monomeric hard spheres, these

---

[3] See Supplemental material at https://www.mdpi.com/journal/polymers

Preprints (www.preprints.org) | NOT PEER-REVIEWED | Posted: 13 September 2022 doi:10.20944/preprints202209.0170.v1

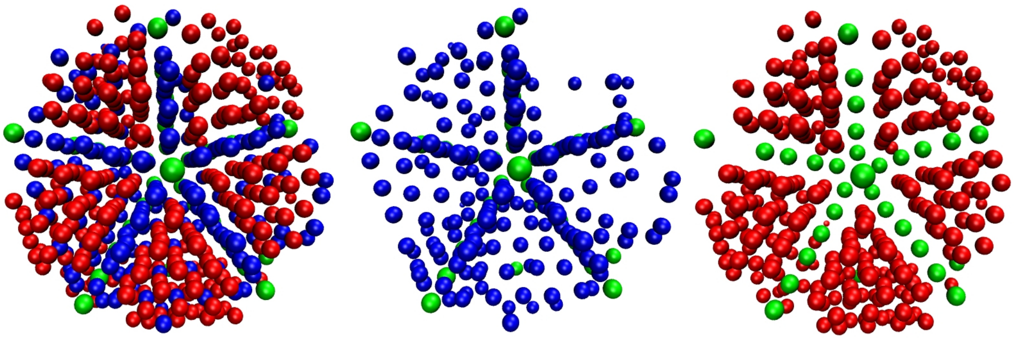

Figure 5. Typical cyclic twin structure (left panel) at frame 1622, early in Region II. View is along the twin axis [110] (perpendicular to the page). The twin axis is occupied by sites with fivefold symmetry; sectors are of mixed HCP (middle panel) and FCC (right panel) character. Only a spherical portion of the simulation cell around the fivefold axis is depicted. Radius of spheres is reduced for clarity. Image created with the VMD visualization software [109].

two polymorphs[4] are separated by a small entropic difference only [34,39–43], i.e. there is no initial overwhelming preference for the formation of the one over the other. As a consequence, and as long as a sufficient pool of amorphous monomers is available, both polymorphs have roughly similar probabilities of being formed. The very large size of the simulation cell offers abundant volume for the independent growth of nuclei of both types of crystals, i.e. there is plenty of available space for both FCC and HCP crystalline regions to grow, as described above, without direct mutual competition.

In Region II the rapid decrease in the number of AMO and FIV and the acompanying growth in crystalline FCC and HCP sites slows down appreciably, especially when compared to the trends observed in Region I. In this region the numbers of FCC, FIV and especially HCP sites remain much more constant, and total crystallinity already exceeds $\approx 60\%$.

Region II is characterized by the competition between HCP and FCC crystalline regions. Region II can be seen as an induction period and is, in a sense, a crucial phase and a stringent test of the efficiency of the MC scheme to properly and efficiently evolve the system towards the stable FCC polymorph, which is separated from HCP and the various rHCP structures by tiny free energy differences only.

The small fraction ($O(10^{-2})$) of FIV sites remaining in Region II have a different character from those in Region I and they are not homogeneouly distributed in space any more. After the rapid disappearance of the initial isolated FIV sites of Region I, the remaining FIV sites associate in almost perfectly linear clusters of $\approx O(10)$ sites. These linear assemblies of FIV sites are the axes of cyclically twinned crystalline domains (see schematic in Fig. 6). In the ideal case, the pentatwins consist of five tetrahedral sectors, each made up of between a few dozens and a hundred monomers. Five such tetrahedra assemble in cyclic twin structures, the axis of which consists of sites with FIV symmetry, while the sectors can have mixed FCC and/or HCP character.

In Region II the number of HCP sites reaches a plateau while the number of FCC monomers grows only slowly and preferentially at the expense of both AMO and FIV sites. The total crystallinity in region II is already appreciable, and most HCP and FCC clusters are contiguous, so that a conversion of crystalline HCP sites into FCC sites would be geometrically possible. In spite of this, it turns out to be easier for the MC scheme to generate new FCC sites from the pool of available AMO sites than to convert neighboring HCP sites into FCC ones. This is consistent with the entropy difference between the amorphous state and both FCC and HCP crystals being larger than the entropy difference between FCC and HCP [96].

---

[4] and all rHCP variations on the stacking theme.

Preprints (www.preprints.org) | NOT PEER-REVIEWED | Posted: 13 September 2022 doi:10.20944/preprints202209.0170.v1

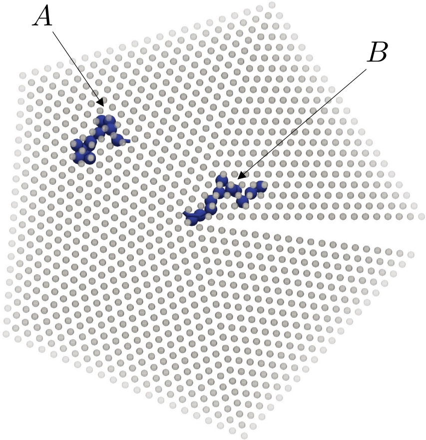

Figure 6. In a cyclic pentatwin (pentagonal bipyramid) chains that span the boundary between twin sectors (A) or pass through the twin axis (B) lose configurational entropy with respect to those in a bulk, untwinned crystal. The white (empty) horizontal wedge is the angular gap of 7.35° left when five equally sized tetrahedra are arranged cyclically around the twin axis (perpendicular to the paper in this figure).

The difficulty of the FCC↔HCP interconversion is also a consequence of the appreciable metastability of the pentatwins: so long as they exist, the composition (HCP and FCC) of their sectors remains basically unchanged, so that HCP sites residing in pentatwin sectors are as immune to transformation into FCC as the twin itself [116]. This is the reason why the proportion of HCP sites does not vary appreciably as long as pentatwins exist.

There is also an extra factor, absent in monomeric systems and specific to chain molecules, that renders most mechanisms of FCC↔HCP interconversion for chains more difficult than for monomeric systems. At first sight, the most straightforward mechanism for HCP $\rightarrow$ FCC conversion is the rearrangement of the stacking . . . A-B-A-B-A-B-. . . →. . . A-B-C-A-B-C-. . . , which would allow FCC crystalline domains to grow at the expense of contiguous HCP domains.

This rearrangement is however totally suppressed in polymer systems because it entails a lateral slide of the (0001) HCP planes along the $\langle 12 \cdot 0 \rangle$ directions. This slide, which is energetically expensive but allowed in monomeric systems [40], is not possible even in principle in a polymer system without breaking the chain backbones.

Easy pentatwin formation, metastability and slide suppression are the main reasons for the relative long life of the HCP polymorph in region II. In spite of the efficiency of the MC scheme it takes a considerable number of steps in the induction regime (plateau Region II in Fig. 1), which correspond to months in wall-clock time, to initiate the final HCP $\rightarrow$ FCC conversion.

The axes of these pentatwins appear as linear assemblies of sites of FIV symmetry, such as those in the right panel of Fig. 4, which shows the spatial distribution of sites with FIV symmetry at frame 1622 in Region II. These compact aggregates of tetrahedra also show up conspicuously as long-lived metastable states in molecular dynamics (MD) simulations of equal-sized spheres [51,52,107,108].

These non-crystallographic structures have repeatedly been observed to form rapidly and then remain almost unchanged for the whole duration of MD simulations, even for monomeric systems. They represent intermediate states of appreciable stability. Their stability stems from the fact that the tetrahedra that compose the pentatwin can all grow simultaneously and independently of each other by accreting further sites from the periphery of the pentatwin. For every new surface layer accreted on the pentatwin, its axis, i.e. the linear assembly of FIV sites grows by one site, and the number of sites in the pentatwin

Preprints (www.preprints.org) | NOT PEER-REVIEWED | Posted: 13 September 2022 doi:10.20944/preprints202209.0170.v1

by $5n_{FIV}(n_{FIV}-1)+1$ sites, where n_{FIV} is the number of FIV sites along the twin axis, without necessitating any change in the existing structure.

As a consequence of their easy formation and growth, ordered, noncrystallographic, metastable aggregates of FIV sites are found not to disappear even in very long MD calculations of monomeric spheres [51,52,107,108]. Very frequently, the system remains trapped in a low free energy basin escaping from which is hard for deterministic dynamic methods.

The present simulation, based on the MC scheme, is able to evolve the system out of this configurational bottleneck. The length of the induction period (Region II) is primarily determined by the slow disappearance of metastable structures having linear assemblies of FIV sites as their axes.

The disappearance of metastable pentatwins is dictated by the impossibility to indefinitely grow into a periodic crystalline structure [5]. If the simulation algorithm is sufficiently efficient and the simulation cell adequately large, they are ultimately superseded by crystalline structure(s) of lower free energy. This evolution is kinetically arrested in most MD simulations, and shows up as a configurational bottleneck in MC methods.

In the present work, the difficulty of evolving the system out of this metastable situation, i.e. of spontaneously resolving the HCP-FCC competition, is marked by the slowdown in the evolution of all types of sites, i.e. the relative flatness of all curves in Region II [6]. The disappearance of FIV sites signals the end of Region II. It is only when the last linear FIV assemblies disappear that crystals resume their growth. The HCP-FCC competition is by then resolved, and HCP regions start transforming into the stable FCC polymorph.

The mechanism of the disappearance of linear FIV assemblies in crystals of polymers is not just by fluctuations brought about by localized rearrangements of sites, as is the case in systems of monomeric hard spheres. In the case of chain molecules the cyclic pentatwin incurs an extra entropic penalty with respect to the untwinned HCP or FCC crystals because its sites are not individual spheres but monomers of a polymeric chain.

There exists an entropic penalty for chains in a cyclic pentatwin caused by the reduced number of available chain conformations with respect to those in a untwinned crystal. In the pentatwin some chains are forced to span the (111) boundaries between sectors (marked with "A" in Fig. 6), or to occupy sites in the $[110]$ twinning axis (the linear FIV assembly, perpendicular to the plane of the paper marked with "B" in Fig. 6). These two geometric situations force some of the torsional angles along the chain to adopt highly improbable values, which entails a decrease in entropy.

In [117] we evaluated the entropic difference between a twinned and a crystalline, but untwinned (bulk) system of hard-sphere chains, and found it to quantitatively explain the almost complete absence of FIV sites in properly equilibrated crystals of hard-sphere polymeric chains.

The magnitudes of these entropic penalties in a pentatwin have been estimated to be $-0.002k$ per monomer for chains spanning (111) sector boundaries and $-0.074k$ per monomer for chains that pass through the $[110]$ twin axis. The former value is comparable to the entropy difference between the HCP and FCC polymorphs for equal monomeric spheres [34,39–43], while the latter is ≈ 35 times larger. These two entropic penalties are thus sufficient to destabilize cyclic twins for chains, in agreement with previous simulation results on hard-sphere chains [73,92,93,118].

Once the induction phase is completed, the numbers of FIV and HCP sites in Region III both drop to zero while the number of FCC monomers grows monotonically up to a maximum of $\approx 93\%$. At the end of Region III the populations of all site types reach an equilibrium state, which signals the onset of the production phase (Region IV) in which all properties fluctuate about well defined average values. Each of the frames in Region IV is a

---

[5] for completeness' sake: the exotic possibility of the appearance of quasicrystalline structures has never been observed in our calculations.

[6] whose duration, measured in wallclock time, was about two years.

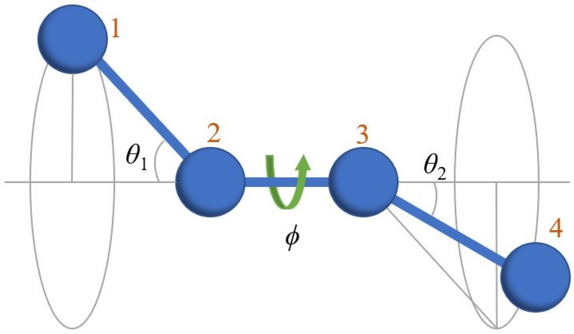

Figure 7. Definition of bending angles θ_1, θ_2 and torsion angle ϕ. The angle ϕ is measured with respect to the plane defined by bonds 1-2 and 2-3.

microstate of the macroscopic, crystalline, stable polymorph, generated with the correct probability from the $[VTN_{sites}\mu^*]$ ensemble.

It is worth emphasizing that in an athermal system like the present one, all configurations that appear, both before and during the production phase, have the same probability $\frac{1}{\Xi}$, where Ξ is the partition function of the $[VTN_{sites}\mu^*]$ ensemble. Since there is no energetic contribution to the free energy, the probability of all *feasible* microstates is identical, whether they correspond to the stable (minimum free energy) macrostate or not. This probability is of course unknown because the isochoric semigrand canonical partition function Ξ cannot be calculated. The difference in entropy (and thus the stability) between the stable polymorph and all other macrostates comes exclusively from the number of microstates that correspond to each macrostate, and not from differences in energy between microstates.

Although also present in thermal systems, this entropic aspect is especially clear in the simulation of athermal systems: the entire evolution and selection of a given polymorph is not related in any way to differences in internal energy U (which can only be 0 or ∞, for feasible or infeasible configurations respectively), but only to the number of feasible configurations. The stable polymorph turns out to be the one with the (overwhelmingly) larger number of microstates. A proper MC scheme generates such microstates with probability $\rightarrow 1$ as $N_{frames} \rightarrow \infty$.

3.2. *Chain statistics and conformations*

An inspection of system frames shows that as the simulation progresses, monomers tend to occupy (on average) the sites of crystalline clusters. This requirement has an impact on the bending and torsional angles of the chain, for chains with unrestricted torsional and bending angles cannot efficiently occupy the sites of a crystal.

The distribution of bending angles (three consecutive monomers joined by two bonds, like monomers 1-2-3, or 2-3-4 in Fig. 7) in the crystal displays a good deal more structure than in the initial, amorphous state. Individual peaks in the distribution in Region IV can easily be assigned to angles formed by two successive bonds joining three sites in the ideal FCC crystal. In particular, the peaks at 60° and 120° are due to parts of the chains laying on sites of the 2D compact hexagonal layers from which the FCC crystal is built up.

The broad peaks in Fig. 8 that correspond to specially simple arrangements of three consecutive monomers which occur with high probability, are shown as sketches in the same figure. The arrows in Fig. 8 mark the values of the bending angles for these simple arrangements. Bending angle values $\approx 30^\circ, 75^\circ$, and 105° are strongly suppressed in the crystal because they do not match the geometry of three consecutive sites along a chain on the FCC crystal.

As Fig. 9 shows, the distribution of torsional angles (ϕ defined by monomers 1-2-3-4 in Fig. 7) in the crystal also strongly deviates from the flat distribution of individual, isolated chains, and also from the distribution of the initial, amorphous configuration at the volume

Preprints (www.preprints.org) | NOT PEER-REVIEWED | Posted: 13 September 2022 doi:10.20944/preprints202209.0170.v1

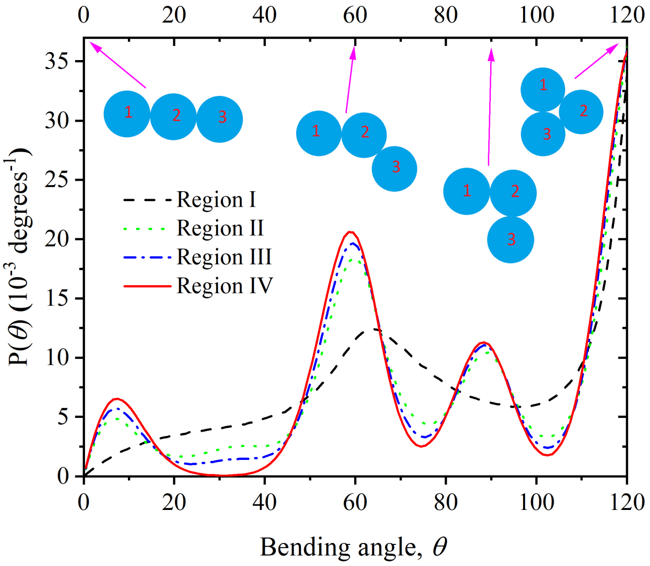

Figure 8. Probability distribution function of bending angles averaged over Regions I through IV. Values of $\theta > 120°$ are forbidden due to overlap of monomers $1-3$. Three-site arrangements that correspond to specific bending angles are sketched as indicated by the arrows. The following color and style format is used throughout the manuscript: Region I (dashed black); Region II (dotted green); Region III (dashed-dotted blue); Region IV (solid red).

fraction $\varphi = 0.56$. Wide, bimodal peaks result from the overlap of closely spaced, favored torsion angles, like 54° and 60°.

The peaks in the torsion angle distribution also correspond to specific conformations of four consecutive monomers (three bonds) whose positions correspond to neighboring sites in an FCC crystal. Some of these four-monomer sequences on the sites of a perfect FCC crystal are sketched along the torsion angle distribution in Fig. 9. The virtually perfect symmetry about $\phi = 0°$ of the distribution in Fig. 9 is further proof of the robust configurational sampling due to the efficiency of the MC protocol and the great length of the simulation. It is further evident that for both bending and torsion angle distributions the minima and maxima become progressively more pronounced as crystal perfection advances, which is consistent with the observation that monomers tend to occupy, within fluctuations, the sites of an FCC crystal.

A key question that arises is whether chains with torsional and bending angles distributions, that so markedly deviate from those in the amorphous state, also have unusual overall conformational properties.

To answer this question, we plot in Fig. 10 the mean squared end-to-end distance $\langle R_{ee}^2 \rangle$ together with 6 times the mean squared radius of gyration $\langle R_g^2 \rangle$, averaged over Regions I and IV. The perfect agreement unequivocally proves ideal chain behaviour within statistical error. A linear fit to the data on the Fig. 10 yields a Flory exponent $\nu = 0.505 \pm 0.004$ (one standard deviation in the mean) in $\langle R_g^2 \rangle \propto l^{2\nu}$, in agreement with ideal chain behavior.

From Fig. 10 it is also possible to deduce that even for the longest chains ($l = 1400$), $\sqrt{\langle R_g^2 \rangle} \approx 19$ which, if taken as a characteristic linear chain size, is quite smaller than the edge of the simulation cell (≈ 37). This confirms that self-interactions through periodic images do not take place, i.e. the appearance of regular, crystalline structures is guaranteed not to be an artifact of the periodic boundary conditions.

A useful measure of chain coiling is given by Kuhn's bond length or by the equivalent freely jointed, phantom chain (i.e. without any kind of excluded volume interactions) [119]. This equivalent phantom chain has the same contour length and the same squared end-to-end distance as the original chain (with excluded volume through Eq.1). In order to

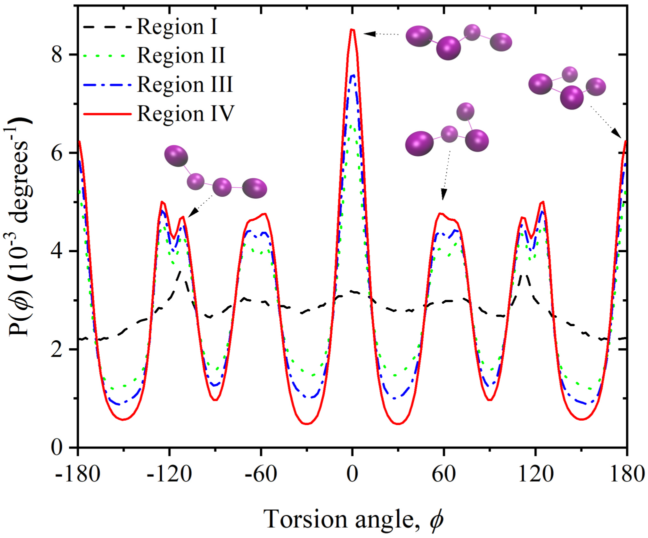

Figure 9. Probability distribution of torsion angles averaged over Regions I through IV. Value of 0° corresponds to the *trans* conformation. Also shown are four-site arrangements that correspond to specific torsion angles as indicated by the arrows.

fulfill these two conditions, the equivalent chain has two degrees of freedom: the number of equivalent segments l' and its bond length, also known as Kuhn length b_0.

From these two conditions:

$$\left.\begin{array}{l} l' b_0 = l\langle b_{len}\rangle \\ l' b_0^2 = \langle |\mathbf{R}_{ee}|^2\rangle \end{array}\right\} \Rightarrow b_0 = \frac{\langle |\mathbf{R}_{ee}|^2\rangle}{l\langle b_{len}\rangle}$$

where $\langle |\mathbf{R}_{ee}|^2\rangle$ is obtained for all chain lengths.

Ideal chain behavior in the crystal may at first sight seem counterintuitive and incompatible with the fact that monomers occupy the sites of a crystal and with the far from uniform distributions of bending and torsion angles. On the one hand, the great length of the chains renders local conformational details imposed by the geometry of the FCC crystal irrelevant, but there is another reason for the chains to display ideal behavior.

As will be qualitatively discussed in the next Section (and quantitatively in a companion paper [96]) the stable macrostate for the polymer system is a crystal because it maximizes the sum of monomer translational entropy, because they occupy the sites of a crystal, and chain conformational entropy, because they adopt ideal conformations compatible with monomers occupying the sites of the crystal. Thus, the crystal results from a combination of maximal positional freedom for the individual monomers about the sites of an ideal crystal, and maximal conformational variability for the entire chains. This result is independent of chain length even for chains of moderate length ($l \approx 10$), which are already in the polymeric regime.

The chains in the present study are far longer. Independent confirmation that all chains in the system are deep in the polymeric regime is also provided by a plot of Kuhn length b_0 as a function of chain length in Regions I and IV (Fig. 11). The independence of Kuhn length b_0 on chain length, indicates that even the shortest ($l = l_{min} = 600$) chains in the system behave as ideal and fully flexible at the scale of the whole chain, and that all chains in the system can be characterized by the same Kuhn length $b_0 = 1.52 \pm 0.05$ (taking the bond length as unit).

The very small value of the Kuhn length (only ≈ 1.5 times the bond length) indicates an extremely high degree of chain coiling. Interestingly, no particular deviation in b_0 is detected between the initial, amorphous state (early part of Region I) and the perfected FCC chain crystal (Region IV), even if the bonded geometry undergoes significant changes during the transition, as demonstrated in Figs. 8 and 9. The only appreciable difference is

Preprints (www.preprints.org) | NOT PEER-REVIEWED | Posted: 13 September 2022 doi:10.20944/preprints202209.0170.v1

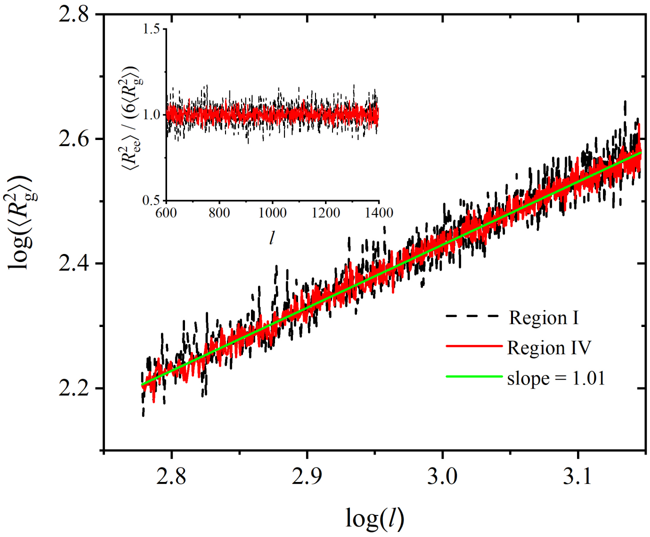

Figure 10. Natural logarithm of the mean square radius of gyration as a function of natural logarithm of chain length for the Regions I and IV. Also shown is a best-fit straight line. (Inset) Mean square end-to-end distance $\langle R_{ee}^2 \rangle$ divided by 6 times the radius of gyration $6\langle R_g^2 \rangle$ as a function of chain length l.

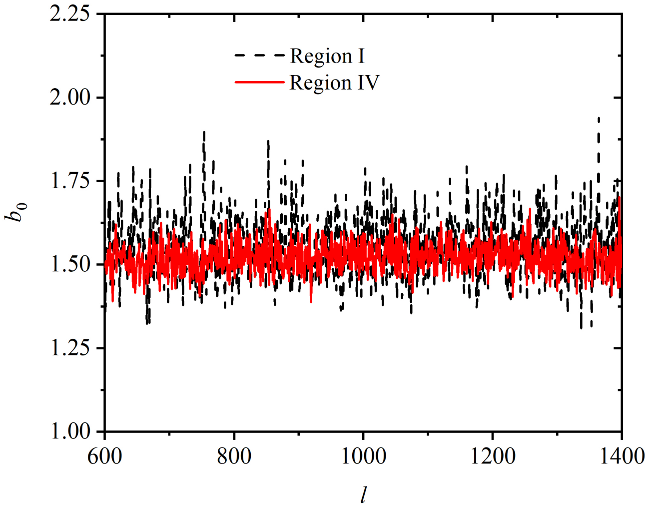

Figure 11. Plot of Kuhn length b_0 as a function of chain length averaged over Regions I and IV. Within statistical uncertainty, the Kuhn length $b_0 = 1.52 \pm 0.05$ is independent of chain length $l \in [l_{min}, l_{max}]$ and the same for both Regions.

Preprints (www.preprints.org) | NOT PEER-REVIEWED | Posted: 13 September 2022 doi:10.20944/preprints202209.0170.v1

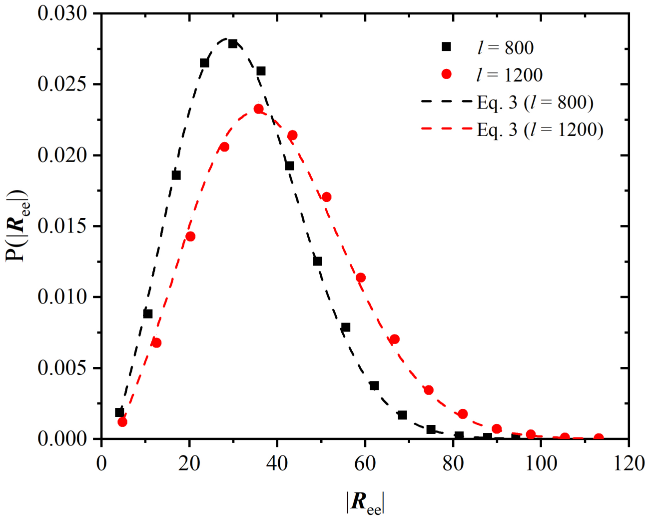

Figure 12. Probability distribution of the modulus of the end-to-end vector, $|\mathbf{R}_{ee}|$ averaged over the production phase, Region IV, for chains of lengths $l = 800 \pm 50$ and $l = 1200 \pm 50$ (small intervals of l instead of single values of l have been used to obtain better statistics), together with the expected distributions according to Eq. (2) setting $b_0 = 1.52$.

the slightly larger variance in the distribution of b_0 (larger fluctuations of the dashed curve in Fig. 11) for different chain lengths, as expected from the greater spatial heterogeneity of the system in the amorphous state (see discussion in the next Section). 513 514 515

Fig. 12 shows the probability distribution function of the end-to-end vector modulus $|\mathbf{R}_{ee}|$ for chains of lengths $l = 800 \pm 50$ and $l = 1200 \pm 50$ (scatter symbols), together with the expected distributions (dashed lines) for the same chain lengths, given by $4\pi|\mathbf{R}_{ee}|^2 f(\mathbf{R}_{ee})$ with:

$$f(\mathbf{R}_{ee}) = \left(\frac{3}{2\pi l b_0}\right)^{\frac{3}{2}} \exp\left(-\frac{3|\mathbf{R}_{ee}|^2}{2lb_0}\right) \tag{2}$$

being the distribution of the end-to-end vector, and $\sigma = 1$ has already been taken into account in (2). In addition, the dashed lines are curves of the same functional form (2) fitted to the distributions obtained from the simulation. 516 517 518

3.3. Entropic Origins of Crystallization 519

The space available to monomers, its homogeneity and its isotropy can conveniently be analyzed by means of the Dirichlet tesselation of space in Voronoi polyhedra based on the coordinates of the monomers, as described in the context of the CCE-norm. 520 521 522

The increase in the regularity of the volume available to the monomers as the crystal is formed can be observed in Fig. 13. This figure shows the probability distribution of the local density (measured as the ratio of the volume of a monomer ($V_{sph} = \frac{\pi}{6}$) to the volume of its Voronoi cell (V_{VC}) for Regions I through IV. 523 524 525 526

Since the $[VTN_{sites}\mu^*]$ ensemble is isochoric, the curves in Fig. 13 have the same mean value, but their shapes and variances do change in the course of the simulation. The wider initial distribution reflects the greater abundance of monomers with either low or high local volume fraction (i.e. high or low volume of their Voronoi cell), while the narrower distribution in Region IV highlights the greater spatial homogeneity (in the sense of the distribution having smaller variance) of the volume of the Voronoi cells in the FCC state. The distribution in Region IV (crystal) follows a Gaussian distribution almost perfectly (dashed line in Fig. 13), which is consistent with the fluctuations of the monomers about the sites of an FCC crystal [120,121]. 527 528 529 530 531 532 533 534 535

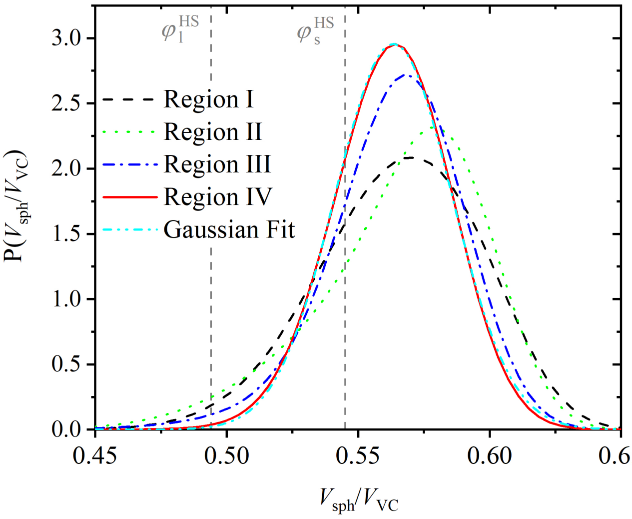

Figure 13. Local volume fraction distribution for the four different Regions. The local volume fraction for a given monomer is defined as the ratio of the volume of a monomer ($V_{sph} = \frac{\pi}{6}$) to the volume of its Voronoi cell V_{VC}. The average of all distributions is identical and coincides with the overall volume fraction $\varphi = 0.56$. The equilibrium distribution (Region IV) follows the Gaussian behavior to excellent accuracy as can be seen by the corresponding fit. Vertical dashed lines mark the volume fractions of the liquid and solid phases of the monomeric HS fluid at equilibrium, $\varphi_l^{HS} = 0.494$ and $\varphi_s^{HS} = 0.545$, respectively.

For reference purposes, the local volume fractions of the liquid and solid phases of the *monomeric* HS fluid at equilibrium are 0.667 and 0.736 times the close-packed density, i.e. $\varphi_l^{HS} = 0.494 \quad (\varphi_l^{*HS} = 0.667)$ and $\varphi_s^{HS} = 0.545 \quad (\varphi_s^{*HS} = 0.736)$, respectively [43,122] (marked with vertical lines in Fig. 13).

A clearer insight into the mechanism of the phase transition is given by the evolution of the volume *accessible* (V_{ac}) to a monomer within its own Voronoi cell. A simple yet convenient definition of accessible volume is that of the region of the Voronoi cell within which the center of the spherical monomer can be placed while keeping its distance to the nearest face of the Voronoi polyhedron < 0.5. Accessible volume in each Voronoi cell is computed by straightforward MC integration. Although much more refined methods exist, like the analytical treatment in [123], the present approach is sufficiently precise for the calculations.

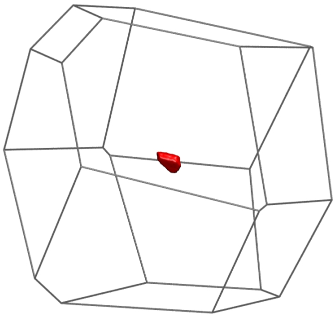

Figure 14. Volume accessible to a monomer with $\varepsilon^{FCC} = 0.18$ within its Voronoi cell. For this monomer: $V_{ac}/V_{VC} = 0.00024$. Accessible volume is colored in red and the Voronoi polyhedron is shown in wireframe representation.

Preprints (www.preprints.org) | NOT PEER-REVIEWED | Posted: 13 September 2022 doi:10.20944/preprints202209.0170.v1

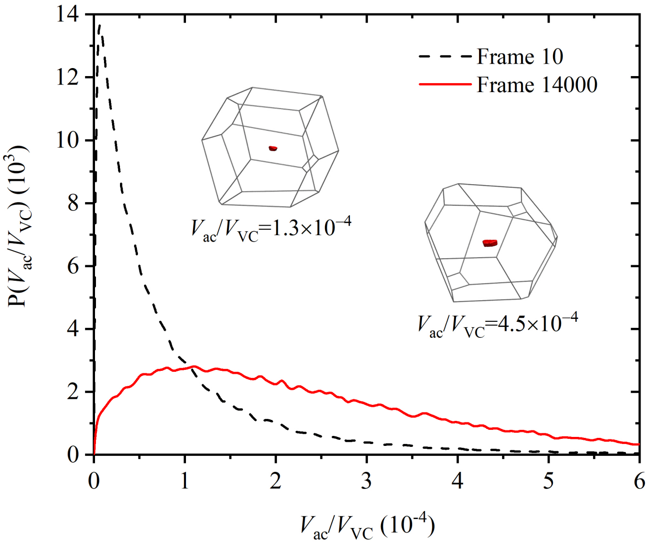

Figure 15. Plot of the relative local accessible volume distribution in the amorphous state (black dashed line) and in the crystalline state (red solid line). Relative accessible volume is the ratio of the local accessible volume of a monomer to the volume of the Voronoi cell of the same monomer. The distributions of the absolute accessible volume follow the same trend. Two snapshots of different accessible volume from sites of the last recorded configuration (frame 1400) are shown as example.

The shape of the accessible volume is a smaller version of the Voronoi polyhedron, but with slightly rounded vertices, and whose faces are parallel to the faces of the Voronoi polyhedron. The logarithm of its size gives, to first order, [124–126] a quantitative measure of the translational entropy of the monomer, under the neglection of multibody correlation and conformational entropy, that is, ignoring the fact that it belongs to a polymeric chain.

Fig. 14 shows a typical Voronoi cell as a wireframe representation, and the accessible volume as the red (medium grey) solid shape within the Voronoi cell.

Unlike the total system volume V, the total accessible volume V_{ac} is not conserved in the $[VTN_{sites}\mu^*]$ ensemble and is very sensitively related to changes in translational entropy. Fig. 15 shows the distribution of the accessible volume for all $N_{sites} = 54000$ monomers, in the initial amorphous state at the beginning of the MC calculation, early in Region I and in the last frame of Region IV, i.e. when the FCC polymorph has fully developed.

While the mean of the distribution of Voronoi cell volume remains constant throughout the calculation, the distribution of accessible volume does become narrower and its mean value shifts to the right. Mean relative accessible volume $\langle V_{ac}/V_{VC}\rangle$ almost triples from 9.0×10^{-5} to 2.5×10^{-4} as the system crystallizes.

Its distribution shows this increase vividly (Fig. 15) and is direct evidence that, by adopting a spatially more homogeneous and geometrically more isotropic arrangement in the crystal, monomers increase their translational freedom and hence the system entropy. This is the main driving force for crystallization of the chains, just as in a system of monomeric hard spheres.

The entropic driving force for crystallization can also be gauged by the correlation between local density and crystal quality, as measured by the CCE norm. Low values of this norm ε^{FCC}, i.e. high local similarity to the perfect FCC crystal, is correlated with high local density, as Fig. 16 demonstrates.

In Fig. 16, data points with ε^{FCC} values below 0.30 have a quite perfect FCC crystalline environment. This numerical value separates the monomers into two non-overlapping clusters, one for non-FCC sites, in which no correlation between density and crystal quality is apparent, and a much more numerous second one in which the correlation between density and crystal quality is very marked. As expected, monomers with almost perfect FCC environment have significantly higher local density.

Preprints (www.preprints.org) | NOT PEER-REVIEWED | Posted: 13 September 2022 doi:10.20944/preprints202209.0170.v1

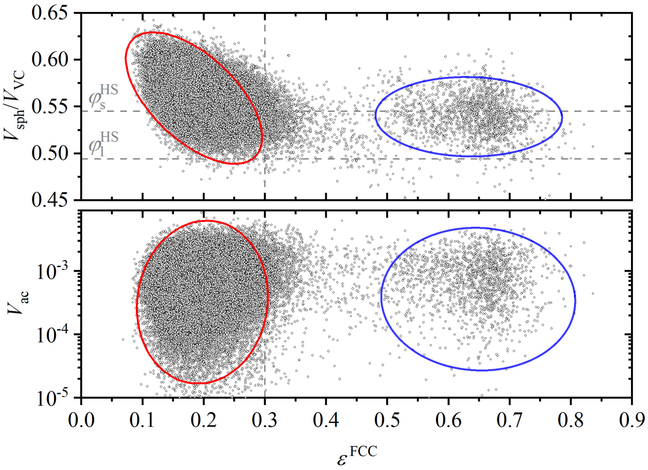

Figure 16. Parity plot of local volume fraction (upper panel) and accesible volume (bottom panel) at a frame 14000 in Region IV *vs.* ε^{FCC}. Red (medium grey) ellipse denotes FCC sites. Blue (dark grey) ellipse corresponds to non-FCC sites. Horizontal dashed lines in the upper panel mark the volume fractions of the liquid and solid phases of the *monomeric* HS fluid at equilibrium, i.e. $\varphi_l^{HS} = 0.494$ and $\varphi_s^{HS} = 0.545$ respectively. The vertical dashed line denotes the CCE-norm threshold $\varepsilon^{thres} = 0.3$.

The bottom panel in Fig. 16 documents the wide range of accessible volumes for FCC sites: the accessible volume V_{ac} for sites of very similar and quite perfect FCC character (with an average $\varepsilon^{FCC} \approx 0.2$) spans a range of two and a half orders of magnitude. This distribution is of course not static: the accessible volume of a given monomer fluctuates along the simulation within the approximate range $[2 \times 10^{-5}, 6 \times 10^{-3}]$ while keeping an almost constant value of ε^{FCC}, i.e. a quite perfect FCC character.

This is in complete agreement with the entropic origin of the transition: even though local density (inversely related to Voronoi cell volume) increases upon crystallization, monomer translational entropy increases because the accessible volume increases on average. The broad distribution for Region I in Fig. 13 (black line) implies that an appreciable number of sites have very small Voronoi cells and hence very little accessible volume (black line in Fig. 15).

During crystallization, Voronoi polyhedra not only become more homogenous in size, (as evidenced by the narrower distribution in Fig. 13 and the shifted distribution in Fig. 15 for Region IV), but also more isotropic. We have monitored the change in Voronoi cell isotropy in two complementary ways.

A first straightforward measure is given by the modulus $|\mathbf{R}|$ of the vector joining the position of a given monomer and the centroid of its Voronoi cell.

As crystallization takes place, not only do the monomer and the centroid of its Voronoi cell tend to be closer together on average (shift to the left in the mean of the distribution of $|\mathbf{R}|$ in Fig. 17), but the distribution of $|\mathbf{R}|$ becomes narrower as well.

A better resolved view in the change of the Voronoi cells is given by shape descriptors derived from the second order gyration tensor, denoted by $\mathbf{G}$. For a given Voronoi polyhedron we define $\mathbf{G}$ as the averaged dyadic of the position vectors of its vertices with respect to the centroid:

$$\mathbf{G} = \frac{1}{N_V}\mathbf{R}\mathbf{R} \tag{3}$$

i.e. the number-averaged analog of the moment of inertia tensor of a set of points of unit mass placed at the vertices of the Voronoi polyhedron.

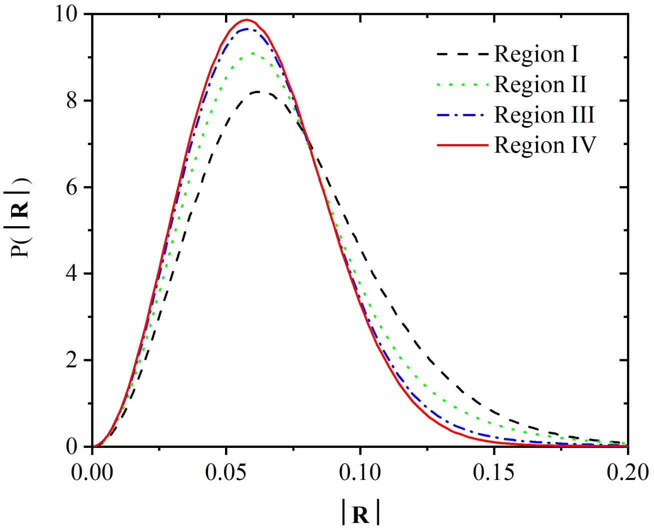

Figure 17. Distributions of $|\mathbf{R}|$,for the four different Regions.

Several scalar shape measures can be extracted from **G**, such as the asphericity b, acylindricity c and the relative shape anisotropy κ^2 coefficient, which are defined respectively by:

$$b = \lambda_1^2 - \frac{1}{2}(\lambda_2^2 + \lambda_3^2) \qquad c = \lambda_2^2 - \lambda_3^2$$
$$\kappa^2 = \frac{3}{2}\frac{\lambda_1^4 + \lambda_2^4 + \lambda_3^4}{(\lambda_1^2 + \lambda_2^2 + \lambda_3^2)^2} - \frac{1}{2} \tag{4}$$

where λ_1^2, λ_2^2 and λ_3^2 are the three eigenvalues of the positive definite **G**, ordered such that $\lambda_1^2 > \lambda_2^2 > \lambda_3^2$.

Notice that while κ^2 is dimensionless, b and c have dimensions of length squared; they are usually made dimensionless by division by $\frac{1}{2}\mathbf{G}$. The lower the values of b, c and κ^2, the more isotropic the shape of the Voronoi polyhedron. An axisymmetric point distribution has $c = 0$, while a spherically symmetric one has $b = c = \kappa^2 = 0$. The Voronoi polyhedron for the FCC crystal, the rhombic dodecahedron, and for the HCP crystal, the trapezo-rhombic dodecahedron, both also have $b = c = \kappa^2 = 0$.

In Fig. 18 we show the evolution of the (dimensionless) b, c and κ^2 along the entire MC simulation. All shape descriptors (4) in Fig. 18 decrease monotonically from the initial values as the simulation evolves (the relative drops are $b \approx 33\%$, $c \approx 17\%$, $\kappa^2 \approx 43\%$), and remain constant (within fluctuations) in Region IV of the stable polymorph. It is remarkable how faithfully all shape descriptors track the evolution of the systems through the four Regions and the final onset of crystallinity. As with accessible volume, the distributions of the shape descriptors (Fig. 19) also get narrower indicating a greater homogeneity of Voronoi cells.

In a rather literal sense, the increase of the accessible volume within Voronoi polyhedra, accompanied by greater uniformity and isotropy, is the force driving the transition from the amorphous to the crystaline state in spite of the opposition due to loss of chain conformational entropy.

4. Conclusions

We have investigated the stability of crystal polymorphs for freely-jointed chains of hard spheres deep in the polymeric regime through unprecedentedly long simulations, based on Monte Carlo algorithms. These simulations shed light on the competition between crystal polymorphs and on crystal perfection. Structural characterization of the local environment around each site allowed for a precise identification of crystal morphologies,

Preprints (www.preprints.org) | NOT PEER-REVIEWED | Posted: 13 September 2022 doi:10.20944/preprints202209.0170.v1

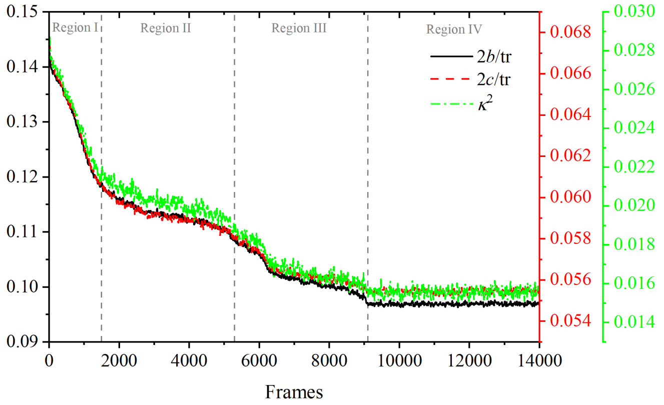

Figure 18. Shape descriptors asphericity b, acylindricity c and relative shape anisotropy κ^2. The first two are made dimensionless by dividing by half the trace of $\mathbf{G}$.

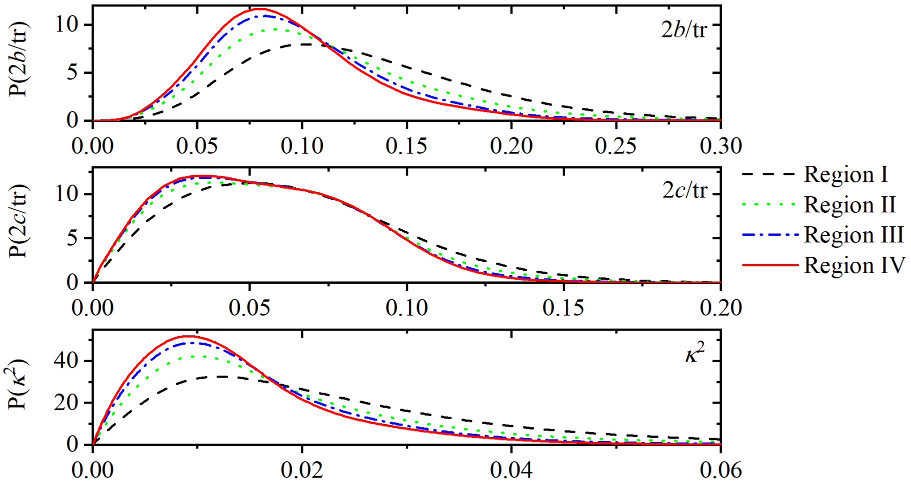

Figure 19. Probability distribution of shape descriptors b, c and κ^2 for Regions I and IV. The first two are made dimensionless by dividing by half the trace of $\mathbf{G}$.

which range from the early, defect-ridden, cyclic twin structures of mixed HCP/FCC type to the final highly perfect, stable FCC crystal.

We find the stable polymorph macrostate to be highly degenerate: all realizations (microstates) of the stable FCC macrostate consist of chains whose monomers tend to occupy, within spatial fluctuations, the sites of the ideal FCC crystal, while maintaining the constraints of chain connectivity and bond length. Polymer chains nevertheless display ideal behavior, as their great length renders local conformational details imposed by the geometry of the FCC crystal irrelevant.

Present simulations allow us to identify the entropic origin of the phase transition: the loss of chain conformational entropy is more than compensated for by the increase in translational entropy as the accessible volume within the Voronoi polyhedra increases.

We have also carried out an analysis of accessible volume that provides further insights into the changes in homogeneity and isotropy of Voronoi cells responsible for the increase in monomer translational entropy. This increase in translational entropy is still large enough to drive the phase transition, in spite of chain conformational loss.

In addition, the present MC results also provide a basis for the calculation [96] of the entropic advantage of the FCC with respect to the HCP polymorph.

The present methodology is currently being extended to tackle semi-flexible athermal polymers in the bulk and under confinement as well as in composites with colloidal nanoparticles.

Author Contributions: Conceptualization, N.C.K and M.L.; methodology, N.C.K, M.L. and K.F.; software, M.H., N.C.K., and K.F.; validation, M.H and K.F.; formal analysis, M.H. and M.L.; data curation, M.H.; writing—original draft preparation, M.H. and M.L.; writing—review and editing, N.C.K. and K.F.; visualization, M.H.; funding acquisition, N.C.K., M.L. and K.F.. All authors have read and agreed to the published version of the manuscript.

Funding: This research was funded by MINECO/FEDER (Ministerio de Economia y Competitividad, Fondo Europeo de Desarrollo Regional) grant numbers MAT2015-70478-P and RTI2018-097338-B-I00 and by UPM and Santander Bank (Programa Propio UPM Santander).

Institutional Review Board Statement: Not applicable

Informed Consent Statement: Not applicable

Data Availability Statement: The presented simulation data are fully available upon request.

Acknowledgments: Very fruitful discussions with Profs. Hans Christian Öttinger, Doros N. Theodorou and Daniel Martinez Fernandez are deeply appreciated. M. H. deeply appreciates the kind hospitality of the COMSE group during his stay in NTUA (Athens, Greece). The authors acknowledge support through projects "MAT2015-70478-P" and "RTI2018-097338-B-I00" of MINECO/FEDER (Ministerio de Economia y Competitividad, Fondo Europeo de Desarrollo Regional). M.H. acknowledges financial support through "Programa Propio UPM Santander" of UPM and Santander Bank. The authors gratefully acknowledge the Universidad Politécnica de Madrid for providing computing resources on the Magerit Supercomputer through projects "r553","r727", "s341", and "u242".

Conflicts of Interest: The authors declare no conflict of interest. The funders had no role in the design of the study; in the collection, analyses, or interpretation of data; in the writing of the manuscript, or in the decision to publish the results.

Abbreviations

The following abbreviations are used in this manuscript:

Preprints (www.preprints.org) | NOT PEER-REVIEWED | Posted: 13 September 2022 doi:10.20944/preprints202209.0170.v1

AMO	Amorphous
BCC	Body-Centered Cubic
CCAMs	Chain-Connectivity-Altering Moves
CCE	Characteristic Crystallographic Element (norm)
FCC	Face-Centered Cubic
FIV	Fivefold
HCP	Hexagonal Close-Packed
HS	Hard Sphere
KMC	Kinetic Monte Carlo
MC	Monte Carlo
MD	Molecular Dynamics
PBC	Periodic Boundary Condition
rHCP	Random Hexagonal Close-Packed
VC	Voronoi Cell

Preprints (www.preprints.org) | NOT PEER-REVIEWED | Posted: 13 September 2022 doi:10.20944/preprints202209.0170.v1

List of variables

b	asphericity
b_{len}	bond length
b_0	Kuhn length
c	acylindricity
dl	mumerical tolerance in bond length
$\mathbf{G}$	second order gyration tensor
I	position index
k	Boltzmann constant
$l, l_{ave}, l_{min}, l_{max}$	Chain length, average, minimum and maximum chain length
n_{dis}	number of trials in configurational bias schemes
n_{FIV}	number of fivefold sites
N	number of polymer chains
N_{frames}	number of frames
N_{sites}	total number of monomeric sites
N_V	number of vertices of the Voronoi polyhedron
r_{ij}	distance between monomers i and j
$\mathbf{r}_m$	position vector of a monomer.
$\mathbf{R}$	displacement from Voronoi Cell centroid vector
R_g	radius of gyration
$\mathbf{R}_{ee}$	end-to-end distance
s	entropy
S^X	order parameter for crystal type X
T	temperature
u_{HS}	hard sphere interaction energy
U	internal energy
$V, V_{ac}, V_{sph}, V_{VC}$	volume, accessible volume, monomer volume, voronoi cell volume
V_a	accessible volume

Greek symbols

Δs_m^{conf}	conformational entropy difference per monomer
Δs_m^{trans}	translational entropy difference per monomer
ε^X	CCE-norm with respect to crystal type X
ϕ	torsion angle
κ^2	relative shape anisotropy
$\lambda_1^2, \lambda_2^2, \lambda_3^2$	eigenvalues of $\mathbf{G}$
φ	volume fraction
φ^*	volume fraction relative to maximum HS packing density (0.7405)
σ	monomer diameter
μ	chemical potential
ν	Flory exponent
τ_c	total crystallinity
θ	bending angle
Ξ	partition function

Preprints (www.preprints.org) | NOT PEER-REVIEWED | Posted: 13 September 2022 doi:10.20944/preprints202209.0170.v1

References

1. Gao, Z.G.; Rohani, S.; Gong, J.B.; Wang, J.K. Recent Developments in the Crystallization Process: Toward the Pharmaceutical Industry. *Engineering* **2017**, *3*, 343–353. https://doi.org/10.1016/j.Eng.2017.03.022.
2. Murray, L.J.; Dinca, M.; Long, J.R. Hydrogen storage in metal-organic frameworks. *Chemical Society Reviews* **2009**, *38*, 1294–1314. https://doi.org/10.1039/b802256a.
3. Janiak, C. Engineering coordination polymers towards applications. *Dalton Transactions* **2003**, pp. 2781–2804. https://doi.org/10.1039/b305705b.
4. Wang, T.; Lu, H.J.; Wang, J.K.; Xiao, Y.; Zhou, Y.A.; Bao, Y.; Hao, H.X. Recent progress of continuous crystallization. *Journal of Industrial and Engineering Chemistry* **2017**, *54*, 14–29. https://doi.org/10.1016/j.jiec.2017.06.009.
5. Li, G.; Zhu, R.; Yang, Y. Polymer solar cells. *Nature Photonics* **2012**, *6*, 153–161. https://doi.org/10.1038/nphoton.2012.11.
6. Koch, F.P.V.; Rivnay, J.; Foster, S.; Muller, C.; Downing, J.M.; Buchaca-Domingo, E.; Westacott, P.; Yu, L.Y.; Yuan, M.J.; Baklar, M.; et al. The impact of molecular weight on microstructure and charge transport in semicrystalline polymer Semiconductors poly(3-hexylthiophene), a model study. *Progress in Polymer Science* **2013**, *38*, 1978–1989. https://doi.org/10.1016/j.progpolymsci.2013.07.009.
7. Meyers, M.A.; Chen, P.Y.; Lin, A.Y.M.; Seki, Y. Biological materials: Structure and mechanical properties. *Progress in Materials Science* **2008**, *53*, 1–206. https://doi.org/10.1016/j.pmatsci.2007.05.002.
8. Mileva, D.; Tranchida, D.; Gahleitner, M. Designing polymer crystallinity: An industrial perspective. *Polymer Crystallization* **2018**, *1*. https://doi.org/10.1002/pcr2.10009.
9. Reiter, G.; Sommer, J. *Polymer Crystallization: Obervations, Concepts and Interpretations*; Springer Berlin Heidelberg, 2008.
10. Russo, J.; Tanaka, H. The microscopic pathway to crystallization in supercooled liquids. *Scientific Reports* **2012**, *2*. https://doi.org/10.1038/srep00505.
11. Erdemir, D.; Lee, A.Y.; Myerson, A.S. Nucleation of Crystals from Solution: Classical and Two-Step Models. *Accounts of Chemical Research* **2009**, *42*, 621–629. https://doi.org/10.1021/ar800217x.
12. Manoharan, V.N. Colloidal matter: Packing, geometry, and entropy. *Science* **2015**, *349*. https://doi.org/10.1126/science.1253751.
13. Palberg, T. Crystallization kinetics of colloidal model suspensions: recent achievements and new perspectives. *Journal of Physics-Condensed Matter* **2014**, *26*. https://doi.org/10.1088/0953-8984/26/33/333101.
14. Pusey, P.N.; Vanmegen, W.; Bartlett, P.; Ackerson, B.J.; Rarity, J.G.; Underwood, S.M. STRUCTURE OF CRYSTALS OF HARD COLLOIDAL SPHERES. *Physical Review Letters* **1989**, *63*, 2753–2756. https://doi.org/10.1103/PhysRevLett.63.2753.
15. Gasser, U.; Weeks, E.R.; Schofield, A.; Pusey, P.N.; Weitz, D.A. Real-space imaging of nucleation and growth in colloidal crystallization. *Science* **2001**, *292*, 258–262. https://doi.org/10.1126/science.1058457.
16. Zhu, J.X.; Li, M.; Rogers, R.; Meyer, W.; Ottewill, R.H.; Russell, W.B.; Chaikin, P.M. Crystallization of hard-sphere colloids in microgravity. *Nature* **1997**, *387*, 883–885.
17. Verhaegh, N.A.M.; Vanduijneveldt, J.S.; Vanblaaderen, A.; Lekkerkerker, H.N.W. DIRECT OBSERVATION OF STACKING DISORDER IN A COLLOIDAL CRYSTAL. *Journal of Chemical Physics* **1995**, *102*, 1416–1421. https://doi.org/10.1063/1.468928.
18. Petukhov, A.V.; Dolbnya, I.P.; Aarts, D.; Vroege, G.J.; Lekkerkerker, H.N.W. Bragg rods and multiple x-ray scattering in random-stacking colloidal crystals. *Physical Review Letters* **2003**, *90*. https://doi.org/10.1103/PhysRevLett.90.028304.
19. Vanmegen, W.; Underwood, S.M. CHANGE IN CRYSTALLIZATION MECHANISM AT THE GLASS-TRANSITION OF COLLOIDAL SPHERES. *Nature* **1993**, *362*, 616–618. https://doi.org/10.1038/362616a0.
20. Pusey, P.N.; Vanmegen, W. PHASE-BEHAVIOR OF CONCENTRATED SUSPENSIONS OF NEARLY HARD COLLOIDAL SPHERES. *Nature* **1986**, *320*, 340–342. https://doi.org/10.1038/320340a0.
21. Russel, W.B.; Chaikin, P.M.; Zhu, J.; Meyer, W.V.; Rogers, R. Dendritic growth of hard sphere crystals. *Langmuir* **1997**, *13*, 3871–3881. https://doi.org/10.1021/la970062b.
22. Cheng, Z.D.; Zhu, J.X.; Russel, W.B.; Meyer, W.V.; Chaikin, P.M. Colloidal hard-sphere crystallization kinetics in microgravity and normal gravity. *Applied Optics* **2001**, *40*, 4146–4151. https://doi.org/10.1364/ao.40.004146.
23. Cheng, Z.D.; Chaikin, P.M.; Zhu, J.X.; Russel, W.B.; Meyer, W.V. Crystallization kinetics of hard spheres in microgravity in the coexistence regime: Interactions between growing crystallites. *Physical Review Letters* **2002**, *88*. https://doi.org/10.1103/PhysRevLett.88.015501.
24. Martelozzo, V.C.; Schofield, A.B.; Poon, W.C.K.; Pusey, P.N. Structural aging of crystals of hard-sphere colloids. *Physical Review E* **2002**, *66*. https://doi.org/10.1103/PhysRevE.66.021408.
25. Kegel, W.K.; Dhont, J.K.G. "Aging" of the structure of crystals of hard colloidal spheres. *Journal of Chemical Physics* **2000**, *112*, 3431–3436. https://doi.org/10.1063/1.480923.
26. Dolbnya, I.P.; Petukhov, A.V.; Aarts, D.; Vroege, G.J.; Lekkerkerker, H.N.W. Coexistence of rHCP and FCC phases in hard-sphere colloidal crystals. *Europhysics Letters* **2005**, *72*, 962–968. https://doi.org/10.1209/epl/i2005-10325-6.
27. Rintoul, M.D.; Torquato, S. Metastability and crystallization in hard-sphere systems. *Physical Review Letters* **1996**, *77*, 4198–4201. https://doi.org/10.1103/PhysRevLett.77.4198.
28. Medvedev, N.N.; Bezrukov, A.; Shtoyan, D. From amorphous solid to defective crystal. A study of structural peculiarities in close packings of hard spheres. *Journal of Structural Chemistry* **2004**, *45*, S23–S30. https://doi.org/10.1007/s10947-006-0092-3.
29. van Meel, J.A.; Frenkel, D.; Charbonneau, P. Geometrical frustration: A study of four-dimensional hard spheres. *Physical Review E* **2009**, *79*. https://doi.org/10.1103/PhysRevE.79.030201.

Preprints (www.preprints.org) | NOT PEER-REVIEWED | Posted: 13 September 2022 doi:10.20944/preprints202209.0170.v1

30. O'Malley, B.; Snook, I. Crystal nucleation in the hard sphere system. *Physical Review Letters* **2003**, *90*. https://doi.org/10.1103/PhysRevLett.90.085702.
31. Punnathanam, S.; Monson, P.A. Crystal nucleation in binary hard sphere mixtures: A Monte Carlo simulation study. *Journal of Chemical Physics* **2006**, *125*. https://doi.org/10.1063/1.2208998.
32. Russo, J.; Tanaka, H. Crystal nucleation as the ordering of multiple order parameters. *Journal of Chemical Physics* **2016**, *145*. https://doi.org/10.1063/1.4962166.
33. Lam, M.A.; Khusid, B.; Kondic, L.; Meyer, W.V. Role of diffusion in crystallization of hard-sphere colloids. *Physical Review E* **2021**, *104*. https://doi.org/10.1103/PhysRevE.104.054607.
34. Pronk, S.; Frenkel, D. Can stacking faults in hard-sphere crystals anneal out spontaneously? *Journal of Chemical Physics* **1999**, *110*, 4589–4592. https://doi.org/10.1063/1.478339.
35. Hales, T.C.; Harrison, J.; McLaughlin, S.; Nipkow, T.; Obua, S.; Zumkeller, R. A Revision of the Proof of the Kepler Conjecture. *Discrete and Computational Geometry* **2010**, *44*, 1–34. https://doi.org/10.1007/s00454-009-9148-4.
36. Auer, S.; Frenkel, D. Numerical prediction of absolute crystallization rates in hard-sphere colloids. *Journal of Chemical Physics* **2004**, *120*, 3015–3029. https://doi.org/10.1063/1.1638740.
37. Sanchez-Burgos, I.; Sanz, E.; Vega, C.; Espinosa, J.R. FCC vs. HCP competition in colloidal hard-sphere nucleation: on their relative stability, interfacial free energy and nucleation rate. *Physical Chemistry Chemical Physics* **2021**, *23*, 19611–19626. https://doi.org/10.1039/d1cp01784e.
38. Leoni, F.; Russo, J. Nonclassical Nucleation Pathways in Stacking-Disordered Crystals. *Phys. Rev. X* **2021**, *11*, 031006. https://doi.org/10.1103/PhysRevX.11.031006.
39. Bolhuis, P.G.; Frenkel, D.; Mau, S.C.; Huse, D.A. Entropy difference between crystal phases. *Nature* **1997**, *388*, 235–236. https://doi.org/10.1038/40779.
40. Bruce, A.D.; Wilding, N.B.; Ackland, G.J. Free energy of crystalline solids: A lattice-switch Monte Carlo method. *Physical Review Letters* **1997**, *79*, 3002–3005. https://doi.org/10.1103/PhysRevLett.79.3002.
41. Mau, S.C.; Huse, D.A. Stacking entropy of hard-sphere crystals. *Physical Review E* **1999**, *59*, 4396–4401. https://doi.org/10.1103/PhysRevE.59.4396.
42. Woodcock, L.V. Entropy difference between the face-centred cubic and hexagonal close-packed crystal structures. *Nature* **1997**, *385*, 141–143. https://doi.org/10.1038/385141a0.
43. de Miguel, E.; Marguta, R.G.; del Rio, E.M. System-size dependence of the free energy of crystalline solids. *Journal of Chemical Physics* **2007**, *127*. https://doi.org/10.1063/1.2794041.
44. Koch, H.; Radin, C.; Sadun, L. Most stable structure for hard spheres. *Physical Review E* **2005**, *72*. https://doi.org/10.1103/PhysRevE.72.016708.
45. Auer, S.; Frenkel, D. Prediction of absolute crystal-nucleation rate in hard-sphere colloids. *Nature* **2001**, *409*, 1020–1023. https://doi.org/10.1038/35059035.
46. Radin, C.; Sadun, L. Structure of the hard sphere solid. *Physical Review Letters* **2005**, *94*. https://doi.org/10.1103/PhysRevLett.94.015502.
47. Noya, E.G.; Almarza, N.G. Entropy of hard spheres in the close-packing limit. *Molecular Physics* **2015**, *113*, 1061–1068. https://doi.org/10.1080/00268976.2014.982736.
48. Zaccarelli, E.; Valeriani, C.; Sanz, E.; Poon, W.C.K.; Cates, M.E.; Pusey, P.N. Crystallization of Hard-Sphere Glasses. *Physical Review Letters* **2009**, *103*. https://doi.org/10.1103/PhysRevLett.103.135704.
49. Valeriani, C.; Sanz, E.; Pusey, P.N.; Poon, W.C.K.; Cates, M.E.; Zaccarelli, E. From compact to fractal crystalline clusters in concentrated systems of monodisperse hard spheres. *Soft Matter* **2012**, *8*, 4960–4970. https://doi.org/10.1039/c2sm25121c.
50. Woodcock, L.V. Entropy difference between the face-centred cubic and hexagonal close-packed crystal structures. *Nature* **1997**, *385*, 141–143. https://doi.org/10.1038/385141a0.
51. Karayiannis, N.C.; Malshe, R.; de Pablo, J.J.; Laso, M. Fivefold symmetry as an inhibitor to hard-sphere crystallization. *Physical Review E* **2011**, *83*. https://doi.org/10.1103/PhysRevE.83.061505.
52. Karayiannis, N.C.; Malshe, R.; Kroger, M.; de Pablo, J.J.; Laso, M. Evolution of fivefold local symmetry during crystal nucleation and growth in dense hard-sphere packings. *Soft Matter* **2012**, *8*, 844–858. https://doi.org/10.1039/c1sm06540h.
53. Luchnikov, V.; Gervois, A.; Richard, P.; Oger, L.; Troadec, J.P. Crystallization of dense hard sphere packings - Competition of HCP and FCC close order. *Journal of Molecular Liquids* **2002**, *96-7*, 185–194. https://doi.org/10.1016/s0167-7322(01)00346-4.
54. Richard, P.; Gervois, A.; Oger, L.; Troadec, J.P. Order and disorder in hard-sphere packings. *Europhysics Letters* **1999**, *48*, 415–420. https://doi.org/10.1209/epl/i1999-00499-9.
55. Chen, H.Y.; Ma, H.R. The density profile of hard sphere liquid system under gravity. *Journal of Chemical Physics* **2006**, *125*. https://doi.org/10.1063/1.2213249.
56. Marechal, M.; Hermes, M.; Dijkstra, M. Stacking in sediments of colloidal hard spheres. *Journal of Chemical Physics* **2011**, *135*. https://doi.org/10.1063/1.3609103.
57. Dasgupta, T.; Edison, J.R.; Dijkstra, M. Growth of defect-free colloidal hard-sphere crystals using colloidal epitaxy. *Journal of Chemical Physics* **2017**, *146*. https://doi.org/10.1063/1.4976307.

58. Hoogenboom, J.P.; van Langen-Suurling, A.K.; Romijn, J.; van Blaaderen, A. Epitaxial growth of a colloidal hard-sphere hcp crystal and the effects of epitaxial mismatch on crystal structure. *Physical Review E* **2004**, *69*. https://doi.org/10.1103/PhysRevE.69.051602.
59. vanBlaaderen, A.; Ruel, R.; Wiltzius, P. Template-directed colloidal crystallization. *Nature* **1997**, *385*, 321–324. https://doi.org/10.1038/385321a0.
60. Senger, B.; Bafaluy, F.J.; Schaaf, P.; Schmitt, A.; Voegel, J.C. CONFIGURATIONS OF ADSORBED HARD-SPHERES AFTER DIFFUSION IN A GRAVITATIONAL-FIELD. *Proceedings of the National Academy of Sciences of the United States of America* **1992**, *89*, 9449–9453. https://doi.org/10.1073/pnas.89.20.9449.
61. Hernandez-Guzman, J.; Weeks, E.R. The equilibrium intrinsic crystal-liquid interface of colloids. *Proceedings of the National Academy of Sciences of the United States of America* **2009**, *106*, 15198–15202. https://doi.org/10.1073/pnas.0904682106.
62. Kosinski, P.; Hoffmann, A.C. Extension of the hard-sphere particle-wall collision model to account for particle deposition. *Physical Review E* **2009**, *79*. https://doi.org/10.1103/PhysRevE.79.061302.
63. McMullen, A.; Holmes-Cerfon, M.; Sciortino, F.; Grosberg, A.Y.; Brujic, J. Freely Jointed Polymers Made of Droplets. *Physical Review Letters* **2018**, *121*. https://doi.org/10.1103/PhysRevLett.121.138002.
64. Verweij, R.W.; Moerman, P.G.; Huijnen, L.P.P.; Ligthart, N.E.G.; Chakraborty, I.; Groenewold, J.; Kegel, W.K.; van Blaaderen, A.; Kraft, D.J. Conformations and diffusion of flexibly linked colloidal chains. *Journal of Physics-Materials* **2021**, *4*. https://doi.org/10.1088/2515-7639/abf571.
65. Zou, L.N.; Cheng, X.; Rivers, M.L.; Jaeger, H.M.; Nagel, S.R. The Packing of Granular Polymer Chains. *Science* **2009**, *326*, 408–410. https://doi.org/10.1126/science.1177114.
66. Brown, E.; Nasto, A.; Athanassiadis, A.G.; Jaeger, H.M. Strain Stiffening in Random Packings of Entangled Granular Chains. *Physical Review Letters* **2012**, *108*. https://doi.org/10.1103/PhysRevLett.108.108302.
67. Liu, Z.G.; Yang, Z.; Chen, X.; Tan, R.; Li, G.; Gan, Z.H.; Shao, Y.; He, J.L.; Zhang, Z.B.; Li, W.H.; et al. Discrete Giant Polymeric Chains Based on Nanosized Monomers. *Jacs Au* **2021**, *1*, 79–86. https://doi.org/10.1021/jacsau.0c00014.
68. Sushko, N.; van der Schoot, P.; Michels, M.A.J. Density-functional theory of the crystallization of hard polymeric chains. *Journal of Chemical Physics* **2001**, *115*, 7744–7752. https://doi.org/10.1063/1.1404390.
69. Vega, C.; McBride, C. Scaling laws for the equation of state of flexible and linear tangent hard sphere chains. *Physical Review E* **2002**, *65*. https://doi.org/10.1103/PhysRevE.65.052501.
70. Shakirov, T. Crystallisation in Melts of Short, Semi-Flexible Hard-Sphere Polymer Chains: The Role of the Non-Bonded Interaction Range. *Entropy* **2019**, *21*. https://doi.org/10.3390/e21090856.
71. Shakirov, T.; Paul, W. Crystallization in melts of short, semiflexible hard polymer chains: An interplay of entropies and dimensions. *Physical Review E* **2018**, *97*. https://doi.org/10.1103/PhysRevE.97.042501.
72. Dietz, J.D.; Hoy, R.S. Two-stage athermal solidification of semiflexible polymers and fibers. *Soft Matter* **2020**, *16*, 6206–6217. https://doi.org/10.1039/d0sm00754d.
73. Karayiannis, N.C.; Foteinopoulou, K.; Laso, M. Entropy-Driven Crystallization in Dense Systems of Athermal Chain Molecules. *Physical Review Letters* **2009**, *103*. https://doi.org/10.1103/PhysRevLett.103.045703.
74. Ni, R.; Dijkstra, M. Effect of bond length fluctuations on crystal nucleation of hard bead chains. *Soft Matter* **2013**, *9*, 365–369. https://doi.org/10.1039/c2sm26969d.
75. Chen, L.T.; Chen, C.Y.; Chen, H.L. FCC or HCP: The stable close-packed lattice of crystallographically equivalent spherical micelles in block copolymer/homopolymer blend. *Polymer* **2019**, *169*, 131–137. https://doi.org/10.1016/j.polymer.2019.02.041.
76. Zhang, C.; Vigil, D.L.; Sun, D.; Bates, M.W.; Loman, T.; Murphy, E.A.; Barbon, S.M.; Song, J.A.; Yu, B.H.; Fredrickson, G.H.; et al. Emergence of Hexagonally Close-Packed Spheres in Linear Block Copolymer Melts. *Journal of the American Chemical Society* **2021**, *143*, 14106–14114. https://doi.org/10.1021/jacs.1c03647.
77. Hsu, N.W.; Nouri, B.; Chen, L.T.; Chen, H.L. Hexagonal Close-Packed Sphere Phase of Conformationally Symmetric Block Copolymer. *Macromolecules* **2020**, *53*, 9665–9675. https://doi.org/10.1021/acs.macromol.0c01445.
78. Mahynski, N.A.; Kumar, S.K.; Panagiotopoulos, A.Z. Relative stability of the FCC and HCP polymorphs with interacting polymers. *Soft Matter* **2015**, *11*, 280–289. https://doi.org/10.1039/c4sm02191f.
79. Mahynski, N.A. Entropic control over nanoscale colloidal crystals. *Molecular Physics* **2016**, *114*, 2586–2596. https://doi.org/10.1080/00268976.2016.1203467.
80. Karayiannis, N.C.; Mavrantzas, V.G.; Theodorou, D.N. A novel Monte Carlo scheme for the rapid equilibration of atomistic model polymer systems of precisely defined molecular architecture. *Physical Review Letters* **2002**, *88*. https://doi.org/10.1103/PhysRevLett.88.105503.
81. Pant, P.V.K.; Theodorou, D.N. Variable Connectivity Method For The Atomistic Monte-Carlo Simulation Of Polydisperse Polymer Melts. *Macromolecules* **1995**, *28*, 7224–7234. https://doi.org/10.1021/ma00125a027.
82. Lebowitz, A.B.M.K.J. A new algorithm for Monte Carlo simulation of Ising spin systems. *Journal of Computational Physics* **1975**, *17*, 10–18. https://doi.org/10.1016/0021-9991(75)90060-1.
83. Fichthorn, Kristen A.; Weinberg, W.H. Theoretical foundations of dynamical Monte Carlo simulations. *The Journal of Chemical Physics* **1991**, *95*, 1090. https://doi.org/10.1063/1.461138.
84. Siepmann, J.I.; Frenkel, D. Configurational bias Monte Carlo - A new sampling scheme for flexible chains. *Molecular Physics* **1992**, *75*, 59–70. https://doi.org/10.1080/00268979200100061.

Preprints (www.preprints.org) | NOT PEER-REVIEWED | Posted: 13 September 2022 doi:10.20944/preprints202209.0170.v1

85. de Pablo, J.J.; Laso, M.; Suter, U.W. SIMULATION OF POLYETHYLENE ABOVE AND BELOW THE MELTING-POINT. *Journal of Chemical Physics* **1992**, *96*, 2395–2403. https://doi.org/10.1063/1.462037.
86. Kroger, M. Efficient hybrid algorithm for the dynamic creation of wormlike chains in solutions, brushes, melts and glasses. *Computer Physics Communications* **2019**, *241*, 178–179. https://doi.org/10.1016/j.cpc.2019.03.009.
87. Shi, W.; Maginn, E.J. Improvement in Molecule Exchange Efficiency in Gibbs Ensemble Monte Carlo: Development and Implementation of the Continuous Fractional Component Move. *Journal of Computational Chemistry* **2008**, *29*, 2520–2530. https://doi.org/10.1002/jcc.20977.
88. Kampmann, T.A.; Boltz, H.H.; Kierfeld, J. Monte Carlo simulation of dense polymer melts using event chain algorithms. *Journal of Chemical Physics* **2015**, *143*. https://doi.org/10.1063/1.4927084.
89. Auhl, R.; Everaers, R.; Grest, G.S.; Kremer, K.; Plimpton, S.J. Equilibration of long chain polymer melts in computer simulations. *Journal of Chemical Physics* **2003**, *119*, 12718–12728. https://doi.org/10.1063/1.1628670.
90. Subramanian, G. A topology preserving method for generating equilibrated polymer melts in computer simulations. *Journal of Chemical Physics* **2010**, *133*. https://doi.org/10.1063/1.3493329.
91. Herranz, M.; Martínez-Fernández, D.; Ramos, P.M.; Foteinopoulou, K.; Karayiannis, N.C.; Laso, M. Simu-D: A Simulator-Descriptor Suite for Polymer-Based Systems under Extreme Conditions. *International Journal of Molecular Sciences* **2021**, *22*, 12464.
92. Karayiannis, N.C.; Foteinopoulou, K.; Abrams, C.F.; Laso, M. Modeling of crystal nucleation and growth in athermal polymers: self-assembly of layered nano-morphologies. *Soft Matter* **2010**, *6*, 2160–2173. https://doi.org/10.1039/b923369e.
93. Karayiannis, N.C.; Foteinopoulou, K.; Laso, M. The role of bond tangency and bond gap in hard sphere crystallization of chains. *Soft Matter* **2015**, *11*, 1688–1700. https://doi.org/10.1039/c4sm02707h.
94. Ramos, P.M.; Herranz, M.; Foteinopoulou, K.; Karayiannis, N.C.; Laso, M. Entropy-Driven Heterogeneous Crystallization of Hard-Sphere Chains under Unidimensional Confinement. *Polymers* **2021**, *13*. https://doi.org/10.3390/polym13091352.
95. Ramos, P.M.; Herranz, M.; Martinez-Fernandez, D.; Foteinopoulou, K.; Laso, M.; Karayiannis, N.C. Crystallization of Flexible Chains of Tangent Hard Spheres under Full Confinement. *Journal of Physical Chemistry B* **2022**, *126*, 5931–5947. https://doi.org/10.1021/acs.jpcb.2c03424.
96. Herranz, M.; Benito, J.; Foteinopoulou, K.; Karayiannis, N.C.; Laso, M. Thermodynamic stability of crystals of hard sphere polymers **2022 (under consideration)**.
97. Laso, M.; Karayiannis, N.C. Flexible chain molecules in the marginal and concentrated regimes: Universal static scaling laws and cross-over predictions. *Journal of Chemical Physics* **2008**, *128*. https://doi.org/10.1063/1.2912189.
98. Karayiannis, N.C.; Laso, M. Monte Carlo scheme for generation and relaxation of dense and nearly jammed random structures of freely jointed hard-sphere chains. *Macromolecules* **2008**, *41*, 1537–1551. https://doi.org/10.1021/ma702264u.
99. Foteinopoulou, K.; Karayiannis, N.C.; Laso, M. Monte Carlo simulations of densely-packed athermal polymers in the bulk and under confinement. *Chemical Engineering Science* **2015**, *121*, 118–132. https://doi.org/10.1016/j.ces.2014.08.021.
100. Ramos, P.M.; Karayiannis, N.C.; Laso, M. Off-lattice simulation algorithms for athermal chain molecules under extreme confinement. *Journal of Computational Physics* **2018**, *375*, 918–934. https://doi.org/10.1016/j.jcp.2018.08.052.
101. Karayiannis, N.C.; Laso, M. Dense and nearly jammed random packings of freely jointed chains of tangent hard spheres. *Physical Review Letters* **2008**, *100*. https://doi.org/10.1103/PhysRevLett.100.050602.
102. Herranz, M.; Santiago, M.; Foteinopoulou, K.; Karayiannis, N.C.; Laso, M. Crystal, Fivefold and Glass Formation in Clusters of Polymers Interacting with the Square Well Potential. *Polymers* **2020**, *12*. https://doi.org/10.3390/polym12051111.
103. Karayiannis, N.C.; Foteinopoulou, K.; Laso, M. The characteristic crystallographic element norm: A descriptor of local structure in atomistic and particulate systems. *Journal of Chemical Physics* **2009**, *130*. https://doi.org/10.1063/1.3077294.
104. Ramos, P.M.; Herranz, M.; Foteinopoulou, K.; Karayiannis, N.C.; Laso, M. Identification of Local Structure in 2-D and 3-D Atomic Systems through Crystallographic Analysis. *Crystals* **2020**, *10*. https://doi.org/10.3390/cryst10111008.
105. Rycroft, C.H. VORO++: A three-dimensional Voronoi cell library in C++. *Chaos: An Interdisciplinary Journal of Nonlinear Science* **2009**, *19*, 041111. https://doi.org/10.1063/1.3215722.
106. Schmidt, M.; Fuchs, M. Penetrability in model colloid-polymer mixtures. *Journal of Chemical Physics* **2002**, *117*, 6308–6312. https://doi.org/10.1063/1.1503303.
107. Hoy, R.S.; Karayiannis, N.C. Simple model for chain packing and crystallization of soft colloidal polymers. *Physical Review E* **2013**, *88*. https://doi.org/10.1103/PhysRevE.88.012601.
108. Nguyen, H.T.; Smith, T.B.; Hoy, R.S.; Karayiannis, N.C. Effect of chain stiffness on the competition between crystallization and glass-formation in model unentangled polymers. *Journal of Chemical Physics* **2015**, *143*. https://doi.org/10.1063/1.4932193.
109. Humphrey, W.; Dalke, A.; Schulten, K. VMD: Visual molecular dynamics. *Journal of Molecular Graphics & Modelling* **1996**, *14*, 33–38. https://doi.org/10.1016/0263-7855(96)00018-5.
110. Mckay, A.L. A dense non-crystallographic packing of equal spheres. *Acta Crystallographica* **1962**, *15*, 916–918. https://doi.org/10.1107/s0365110x6200239x.
111. Bagley, B.G. A Dense Packing of Hard Spheres with Five-fold Symmetry. *Nature* **1965**, *208*, 674–675. https://doi.org/10.1038/208674a0.
112. Bagley, B.G. 5-Fold Pseudosymmetry. *Nature* **1970**, *225*, 1040–&. https://doi.org/10.1038/2251040a0.

Preprints (www.preprints.org) | NOT PEER-REVIEWED | Posted: 13 September 2022 doi:10.20944/preprints202209.0170.v1

113. Anikeenko, A.V.; Medvedev, N.N.; Bezrukov, A.; Stoyan, D. Observation of fivefold symmetry structures in computer models of dense packing of hard spheres. *Journal of Non-Crystalline Solids* **2007**, *353*, 3545–3549. https://doi.org/10.1016/j.jnoncrysol.2007.05.113.
114. Kuo, K.H. Mackay, Anti-Mackay, Double-Mackay, Pseudo-Mackay, and Related Icosahedral Shell Clusters. *Structural Chemistry* **2002**, *13*, 221–230. https://doi.org/10.1023/a:1015847520094.
115. Anikeenko, A.V.; Medvedev, N.N. Polytetrahedral nature of the dense disordered packings of hard spheres. *Physical Review Letters* **2007**, *98*. https://doi.org/10.1103/PhysRevLett.98.235504.
116. Ni, R.; Dijkstra, M. Effect of bond length fluctuations on crystal nucleation of hard bead chains. *Soft Matter* **2013**, *9*. https://doi.org/10.1039/C2SM26969D.
117. Karayiannis, N.C.; Foteinopoulou, K.; Laso, M. Twinning of Polymer Crystals Suppressed by Entropy. *Symmetry-Basel* **2014**, *6*, 758–780. https://doi.org/10.3390/sym6030758.
118. Karayiannis, N.C.; Foteinopoulou, K.; Laso, M. Spontaneous Crystallization in Athermal Polymer Packings. *International Journal of Molecular Sciences* **2013**, *14*, 332–358. https://doi.org/10.3390/ijms14010332.
119. Flory, P.J. *Statistical Mechanics of Chain Molecules*; Hanser-Verlag: Munchen, 1989.
120. Neil W. Ashcroft, N.D.M. *Solid state physics*, 1 ed.; Solid State Physics, Holt, Rinehart and Winston, 1976.
121. Dove, M.T. *Introduction to Lattice Dynamics*; Cambridge Topics in Mineral Physics and Chemistry 4, Cambridge University Press, 1993.
122. Hoover, W.G.; Ree, F.H. Melting Transition And Communal Entropy For Hard Spheres. *Journal of Chemical Physics* **1968**, *49*, 3609–&. https://doi.org/10.1063/1.1670641.
123. Dodd, L.R.; Theodorou, D.N. Analytical treatment of the volume and surface area of molecules formed by an arbitrary collection of unequal spheres intersected by planes. *Molecular Physics* **1991**, *72*, 1313–1345. https://doi.org/10.1080/00268979100100941.
124. Irving, J.H.; Kirkwood, J.G. The statistical mechanical theory of transport processes. IV. The equations of hydrodynamics. *J. Chem. Phys.* **1950**, *18*, 817–829.
125. Kumar, V. Senthil; Kumaran, V. Voronoi neighbor statistics of hard-disks and hard-spheres. *The Journal of Chemical Physics* **2005**, *123*, 074502. https://doi.org/10.1063/1.2000233.
126. Kumar, V.S.; Kumaran, V. Voronoi cell volume distribution and configurational entropy of hard-spheres. *Journal of Chemical Physics* **2005**, *123*. https://doi.org/10.1063/1.2011390.